5-1-2011

Experimental study of pool boiling heat transfer enhancement over microchanneled surfaces

Dwight Cooke

Experimental Study of Pool Boiling Heat Transfer Enhancement over Microchanneled Surfaces

By

Dwight Cooke

A Thesis Submitted in Partial Fulfillment of the Requirement for Master of Science in Mechanical Engineering

Approved by:

Dr. Satish G. Kandlikar
Department of Mechanical Engineering _____
(Thesis Advisor)

Dr. Robert J. Stevens
Department of Mechanical Engineering _____
(Examiner)

Dr. Steven W. Day
Department of Mechanical Engineering _____
(Examiner)

Dr. Wayne W. Walter
Department of Mechanical Engineering _____
(Department Representative)

Rochester Institute of Technology
Rochester, New York 14623
May 2011

Permission to Reproduce The Thesis

Experimental Study of Pool Boiling Heat Transfer Enhancement over Microchanneled Surfaces

I, Dwight Cooke, hereby grant permission to the Wallace Memorial Library of Rochester Institute of Technology to reproduce my thesis in the whole or part. Any reproduction will not be for commercial use or profit.

May 2011

_____

Signature of Author

Abstract

Pool boiling is of interest in heat transfer applications because of its potential for removing large amount of heat resulting from the latent heat of evaporation and little pressure drop penalty for circulating coolant through the system. However, the heat transfer performance of pool boiling systems is still not comparable to the cooling ability provided by enhanced microchannels operating under single-phase conditions. This investigation focuses on the bubble dynamics and heat transfer on plain and structured microchanneled surfaces under various heat fluxes in an effort to understand the underlying heat transfer mechanism through the use of a high speed camera.

In a preliminary study, silicon chips have been tested in the nucleate boiling regime, and beneficial microchannel geometries have been identified. It is determined that heat transfer enhancement occurs because of (i) an increase in surface area and (ii) an improvement in the heat transfer mechanism through the channels functioning as liquid conduits for three side heating. The range for channel size in which the greatest enhancement occurs has been identified as being 200 – 400 μm width and 300 – 500 μm depth.

The second study has been investigated with copper chips, with improvements to the test setup for accurate measurement of surface temperature. Ten chips, in addition to a plain chip have been evaluated for heat transfer performance. It has been determined that surfaces with many, small hydraulic diameter channels enhance the heat transfer as well as surfaces with wide and deep channels. The best performing chip had a record heat transfer coefficient of 269 kW/m^2K. The large heat fluxes of over 240 W/cm^2 were attained without reaching the critical heat flux condition, because of the open channels on the surface acting as conduits for liquid supply to the nucleation sites. The microchannels prevent surface dryout and critical heat flux (CHF), while the channel width controls the size of the departing bubbles.

List of Figures

List of Tables

Nomenclature

a_i	measured parameter
h_{lv}	latent heat, J/kg
h	distance from bottom of channel to bottom of bubble, μm
H	channel height/depth, μm
k	thermal conductivity, W/mK
L	length, m
q''	heat flux, W/m^2
r	cavity radius, m
R	bubble radius, m
$R''_{t,c}$	thermal contact resistance, m^2K/W
R_{tot}	sum of resistances, m^2K/W
T	temperature, K
U	uncertainty
B	bias error
p	pressure, N/m^2
P	precision error
P	parameter
W	channel width, μm
x	distance, m

Greek Symbols

ΔT_{sat}	wall superheat, K
ΔT_{sub}	liquid subcooling, K
δ_t	thermal boundary layer length, m
θ	contact angle, degrees
v_{lv}	liquid-vapor specific volume difference, m^3/kg
σ	surface tension, N/m

Table of Contents

1. Introduction

Heat transfer, in particular the cooling aspect is of great importance to engineering applications. Failure to properly cool devices and materials can lead to improper operation or material degradation and failure. Two of the simplest cooling approaches are air cooling and liquid cooling. From each of these cooling methods the fluid (gas of liquid) can be utilized by natural convection or by forced convection. Table 1.1 shows the various cooling methods along with typical values for heat transfer coefficients.

Table 1.1 Cooling methods and typical heat transfer coefficients [2]

Cooling Method	h [W/m^{2}K]
Natural Convection – Air	2 - 25
Forced Convection – Air	25 - 250
Natural Convection – Water	50 - 1,000
Forced Convection – Water	100 - 20,000
Boiling	2,500 - 100,000

Pool boiling is defined as a liquid-vapor phase change with a quiescent liquid, where fluid motion is due to free convection and from bubble growth and departure. During pool boiling, the effects of the latent heat involved with the phase change from liquid to vapor become significant. The substantial increase in the heat transfer coefficient allows for pool boiling being a candidate for cooling applications in high powered electronics and in cooling for nuclear applications. It is a technique which does not require any moving parts and is highly effective from both the thermal and cost perspectives.

1.1 Bubble Nucleation

In order for bubbles to take place, certain conditions must be met, shown in Fig. 1.1. A heated surface in a pool of liquid with a temperature that is greater than the saturation temperature for a fluid will develop a boundary layer of superheated liquid next to that layer. On the heated surface, cavities with entrapped vapor may exist, with the vapor embryos providing the first bubbles for nucleation. For the vapor to grow, the temperature of the liquid surrounding the vapor must be greater than the saturation temperature corresponding to the vapor pressure inside the bubble. For a stationary bubble in a fluid, two forces are present – surface tension and pressure. With the sum of the forces equal to zero, the force balance is shown by Eq. (1.1):

$$\pi R^2 \left(p_v - p_l\right) - 2\pi R\sigma = 0 \tag{1.1}$$

Moving the terms around, the vapor pressure inside the bubble can be represented as a function of the hydraulic pressure, surface tension of the fluid and the bubble radius:

$$p_v = p_l + \frac{2\sigma}{R} \tag{1.2}$$

Equation (1.2) is interesting in that the vapor pressure is dependent on the bubble radius. For small bubbles, the vapor pressure is high, so for the bubbles to grow the corresponding saturation temperature will be higher than for the fluid at pressure, p_v. This shows that a surface must have a wall superheat for bubble nucleation and growth.

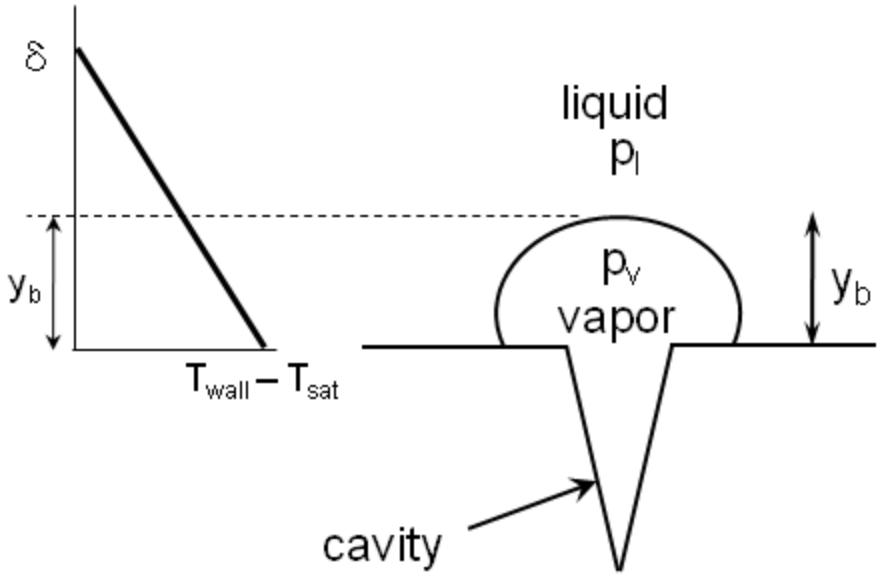

Figure 1.1. Nucleation criteria for bubble growth

1.2 Boiling Curve

The boiling curve is used to quantify the abilities of a surface for heat dissipation through boiling. Shown in Fig. 1.2, the boiling curve plots the heat flux versus the wall superheat. The first portion of the curve, up to point A is where natural convection takes place, before the surface has attained the required superheat for nucleation. Between points A and C, there is nucleate boiling, with transition point B which represents the point at which vapor bubbles begin to coalesce with adjacent bubbles after nucleating. Point C is the point of critical heat flux (CHF) and represents the point of maximum heat transfer. This is when the most evaporation takes place with liquid still able to rewet the surface. After this point transition and film boiling take place, where areas of the heater experience dryout due to so much evaporation occurring the liquid is not able to rewet the surface.

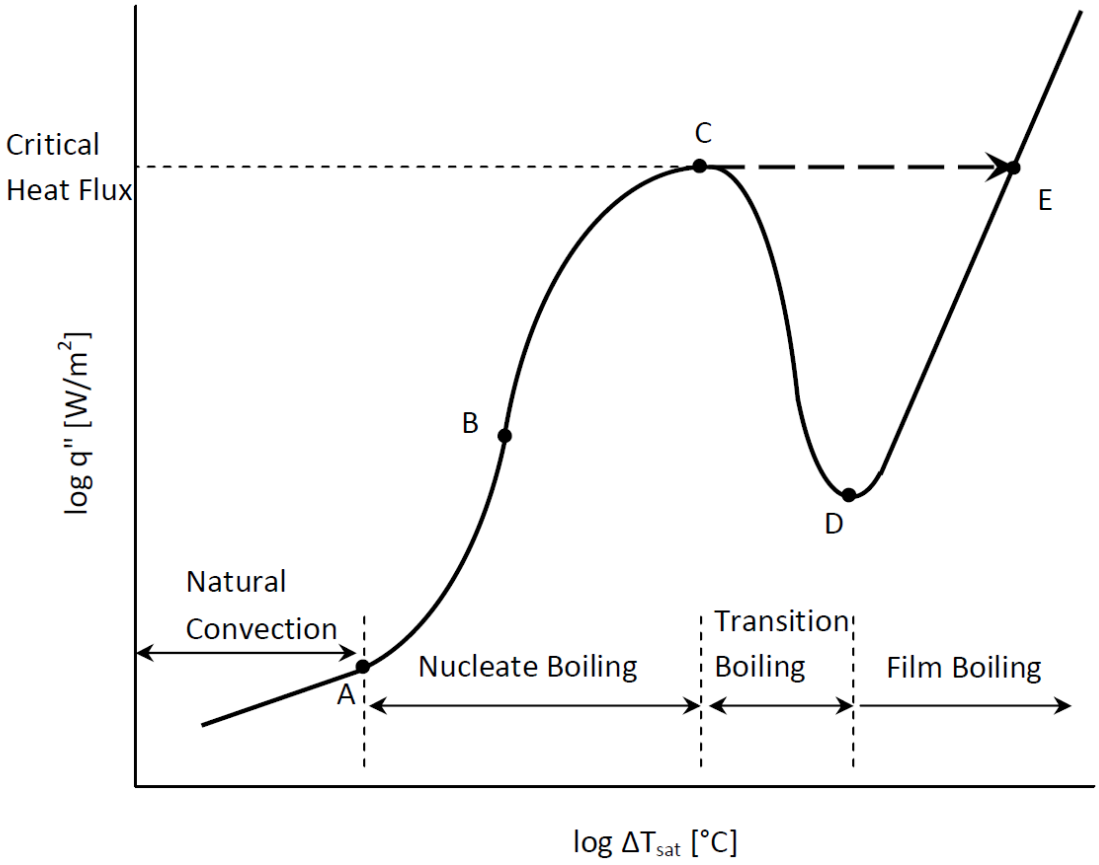

Figure 1.2. Typical boiling curve

Depending on the heating method, one of two things will occur after point C. In power controlled heating, as in supplying an electrical current to a resistive metal, the heat flux is the independent variable. In this case the boiling curve will have a large spike in temperature after the CHF condition and the curve will move to point E. When decreasing the heat flux from point E, film boiling will continue until it reaches the minimum heat flux (MHF) at point D. At this point the wall superheat will decrease drastically at the same heat flux, returning to the portion of the curve in the nucleate boiling regime. In this study, temperature controlled heating is used, with heat applied through a copper block. After CHF is reached, as vapor covers more and more of the surface in transition boiling, the heat

dissipated from the surface decreases, while the temperature increases to point D in the figure. Additional increases in temperature will increase the heat flux to point E. Decreasing the wall superheat will follow the curve the same way back to point C and into nucleate boiling.

It is of great importance to clearly understand the boiling phenomenon – failure to know the limitations of a particular surface could cause dryout at the critical heat flux (CHF) condition, which leads to a spike in wall temperature, decreased heat transfer, and possible material failure. Therefore, the mechanisms and behavior of bubble nucleation, evaporation growth, as well as the rewetting of the surface are of great importance and are pursued by many researchers.

2. Literature Review

2.1 Early Studies

Nukiyama [3] was the first to gain insight into the boiling heat transfer phenomena. Using a power controlled nichrome wire, he was able to develop the boiling curve by plotting the heat flux vs. wall superheat. Nukiyama also identified the boiling regimes as free convection, nucleate (jets and columns), transition and film boiling. He found that as the surface temperature of the heater increased, so did the heat flux. However, there did exist an inflection point where increases in temperature would increase the heat flux, but with diminishing returns. At the point where the heat flux reached a maximum, the boiling regime turned from nucleate to transition boiling. This maximum heat flux, termed the critical heat flux (CHF) is of great interest, because of possible material failure due to the high temperatures.

Rohsenow [4] developed a correlation to relate the wall superheat to the heat flux within the nucleate boiling regime. He used a surface-fluid coefficient, $C_{s,f}$ for various combinations. Cooper [5] also developed a correlation for nucleate pool boiling, incorporating the molecular weight of the fluid and surface roughness.

Bubble nucleation has received much attention from researchers in an effort to explain how and where bubbles will nucleate. Early on, it was noticed that the wall superheat must be greater than the saturation temperature of the fluid, about 5°C for water. Hsu and Graham [6] and Hsu [7] developed the criterion for active nucleation sites. They found that the maximum and minimum possible active cavity sizes were functions of subcooling,

pressure and the length of the thermal boundary layer. Since the heat transfer in pool boiling is intimately associated with the contact line and interface movements, microscale surface modification of the heater surface is expected to directly affect the heat transfer phenomena.

2.2 Imaging

As a non-intrusive technique, high speed cameras have been employed with increasing use in recent years. Siedel et al. [8] used high speed imaging of pentane boiling to observe bubble interactions between nucleation sites. In their study, a copper plate was indented with a 180 μm diameter cavity for single bubble studies, and a second cavity was added to observe multiple bubble interactions. It was found that the bubbles produced were not spherical, so instead of bubble departure diameter, bubble departure volume was used for characterization. When bubble coalescence occurs, the microlayer under the bubbles is eliminated due to capillary forces, and is not responsible for an increase in vapor generation. The authors found the bubble frequency is proportional to the wall superheat.

Chung and No [9] conducted a visualization study on how the critical heat flux (CHF) condition is reached. They studied R-113 bubble growth visually from both underneath their heater as well as a side view of the bubbles. They concluded that the CHF condition is attained when the dry area of the heater is above 70%, with additional heat flux causing the dry spots to grow further, which increases the heater surface temperature.

Zhang and Shoji [10] conducted experiments with artificial cavities, imaging the interactions between nucleating bubbles. By changing the separation between the 10 μm diameter cavities, the authors concluded that there are four categories for ratios of separation

to bubble departure diameter. As the separation to departure diameter decreased, the departure frequency was influenced by first the hydrodynamic interaction between bubbles, the thermal interaction between sites, and lastly by the horizontal and declining coalescences.

Ghiu and Joshi [11] visualized confined pool boiling with both single and double layer microchannels of various channel widths. By placing a quartz top cover, they were able to visualize the liquid-vapor dynamics within the microchannel. They observed a pattern of oscillations for the vapor slugs in the top and bottom channels due to the evaporation of the liquid and rewetting of the heated surface.

2.3 Heat Transfer Enhancement – Surface Enhancement

In recent years, many researchers have focused on surface enhancements to promote bubble nucleation and increased heat transfer. Mitrovic and Hartmann [12] created a micropin surface, with elements that were cylindrical in shape, some with a torospherical top. Conducting tests in a pool of R141b, they used various pin diameters (0.8 – 23 μm) and densities (450 – 90,000 pins per mm^2). They found the microstructures effectively increased the heat transfer capabilities compared to the smooth surface. Similarly, Wei and Honda [13] used square pin fins on silicon chips immersed in subcooled FC-72 to observe the effects of pin size and height on heat transfer. The authors concluded the fins enhanced the maximum heat flux by 4.2 times while maintaining the chip temperature below 85°C. Hübner and Künstler [14] investigated the heat transfer enhancement due to trapezoidal, T-shaped, and Y-shaped fins. They also investigated the effects of surface roughness on these structures using sandblasting or emery paper techniques independently. It was found that trapezoidal

fins only increased bubble formation because of a very rough top surface (artifact from machining). However, the T and Y - shaped fins were responsible for increasing the heat transfer coefficient significantly.

Some investigators have looked into using microporous coatings as a means of enhancement [15-18]. Chang and You [15, 16] boiled FC-72 using various porous coatings and thicknesses for both thermally conductive and nonconductive particles [15] as well as microporous coatings such as aluminum, copper, diamond and silver [16]. It was determined that the porous material increased the number of active nucleation sites, and was able to delay the transition to film boiling, thereby enhancing the boiling curve. Rainey et al. [18] applied to a 5 x 5 grid of 1 mm x 1 mm square pin fins. They used copper with varying pin sizes and investigated the CHF values for subcooled boiling with and without the microporous coatings. They found that an increase in pressure can increase performance and increased subcooling shifts the boiling curve upward.

To evaluate the performance of various cavity and reentrant cavity geometries, Das et al. [19] used wire EDM to create tunnels in a copper block. These tunnels were inclined or normal to the heating surface, had rounded, rectangular, or circular bases and were parallel or orthogonally intersecting as well. For the nucleate pool boiling with distilled water, the authors concluded that tunnels inclined from the surface had higher heat transfer compared to ones normal to the surface. The same was true for the circular reentrant cavities, as well as for the orthogonal intersecting tunnels.

In a subsequent publication, Das et al. [20] used a copper surface with 600 μm diameter, 2 mm deep holes. The group varied the spacing of the holes with 5 mm, 7.5 mm and 10 mm pitches. The voltage and current of cartridge heaters were used to calculate the

heat flux, while a thermocouple was placed 1.5 mm below the test surface to measure the average temperature of the test block. The study showed heat fluxes of 465 W/cm^2 at a wall superheat of 16.8 °C. For holes that are 2 mm deep, the temperature should be corrected to account for the higher temperature at the bottom of the holes. At a heat flux of 465 W/cm^2 for a 2 mm distance in copper, the surface temperature would change to be over 23.2 °C higher than the top surface, which would bring the actual wall superheat at the bottom of the hole to 40 °C.

Using microchannel meshes created out of silicon, Ramaswamy et al. [21] conducted an experimental study, focusing on varying pore size, pitch and height. In an effort to study the bubble departure diameter, growth rate, frequency and site density from a porous layer, a 3D structure was used for boiling enhancement. The 3D structures were composed of two layers of microchannels, 0.51 mm thick, positioned 90° from one another, similar to the structures of [11]. The authors obtained boiling curves for different pore sizes, pore pitches, and stack heights. The enhancements caused by stacking multiple structures was found to only have a significant effect at low wall superheats, diminishing at higher temperatures. It was thought that this could be because of a fin effect as height increased in the stack. In addition to increasing the stack height, increasing the pore size, or decreasing the pore pitch increased the heat transfer.

Carbon nanotubes (CNTs) are another promising candidate for enhancing the heat transfer in pool boiling. Launay et al. [22] investigated numerous surfaces, including smooth silicon, rough silicon, CNT coated surfaces, pin fin surfaces, as well as 3D structure surfaces with and without CNTs. The 3D structures were two layers of silicon microchannels, positioned 90° from one another, similar to that of [11] and [21]. The results from the

experiments were that the 3D microchannel structures performed the best, and the addition of CNTs only slightly improved the heat transfer at the lower superheated wall temperatures.

2.4 Heat Transfer Enhancement - Surface Wettability and Contact Angle

Some researchers have changed the way a fluid behaves on a heated surface, producing enhancements. In an early study, Liaw and Dhir [23] used a vertical heater for pool boiling experiments for saturated water. They used a copper surface and changed the static contact angle of the water on it, by varying the level of oxidation. After producing boiling curves for surfaces with contact angles from 14° to 90°, it was determined that as the contact angle is decreased, the boiling curve shifts to the right, but the value for critical heat flux increases.

Similarly, Takata et al. [24] used titanium dioxide (TiO_2) to change the wettability of a surface. Without any treatment, the TiO_2 surface is hydrophobic, but when exposed to ultraviolet light, the TiO_2 surface becomes hydrophilic. Depositing droplets of water on these surfaces when heated, the hydrophilic surfaces have a much quicker evaporation time than the hydrophobic surfaces. This suggested that the hydrophilic surface was the better surface for heat transfer. This conclusion was supported by comparing the surfaces under pool boiling conditions, in which the hydrophilic surface was able to attain much higher heat fluxes than the hydrophobic surface.

Other ways to vary contact angle is through nanocoating. By depositing various particles on a stainless steel substrate, Phan et al. [25] were able to create seven surfaces to vary the contact angle from 22° to 112°. They found that hydrophobic surfaces produce

bubble nucleation at lower wall superheats compared to the hydrophilic surfaces, but bubbles coalesce to create vapor blankets that cover the surface at low wall superheats, thereby inducing critical heat flux. The authors also found that the heat transfer coefficient increased for surfaces with contact angles close to 90° and close to 0°. The surface which had a contact angle of 67° had the worst performance, but the authors speculated that a surface with a contact angle of 45° would underperform more.

Nanowires have also been able to improve heat transfer performance by changing the contact angle. Chen et al. [26] investigated silicon nanowires and copper nanowires that decreased the contact angle from 40° on plain silicon, to about 0° with the nanowires. The copper nanowire surface was able to attain a higher CHF value than the silicon nanowires, at just over 220 W/cm^2. Compared to a plain silicon surface, the enhancement was over 100% for both the CHF value and the heat transfer coefficient.

Both hydrophobic and hydrophilic surfaces have certain advantages and disadvantages for boiling heat transfer. By introducing a surface that has both hydrophobic and hydrophilic areas, Betz et al. [27] were able to show significant heat transfer improvement. On a silicon wafer, they deposited SiO2 buffered with hydrofluoric acid for hydrophilic regions, and PTFE dots for hydrophobic regions. They found that the best performing surface was a hydrophilic network, a surface mostly hydrophilic but with hydrophobic islands spaced throughout.

2.5 Heat Transfer Enhancement - Porous Media

Porous media have also been employed for pool boiling enhancement. Many porous surfaces have been studied [28-31] and found to dissipate high heat fluxes at lower wall temperatures compared to a plain surface. Also, the porous foam has shown to initiate bubble nucleation at very low temperatures. Many of these studies have focused on optimizing the foam for the number of pores per inch (ppi), thickness of the foam, porosity and material selection.

Chang and You [28] experimentally investigated the use of various material particles (aluminum, copper, diamond, and silver) between 1 – 50 μm as a porous epoxied material to a heated surface. It was found that the application of microporous coatings increased the number of active nucleation sites, thereby increasing the heat flux for a given wall superheat. For nucleate boiling this enhancement was about 30% and the CHF value increased by about 100%.

Yang et al. [29] used water as the working fluid with a copper foam, and characterized the boiling heat transfer process. At large heat fluxes, the boiling mode is dominated either by the resistance to vapor release by the foam or the ability of the foam to have a capillary wicking mechanism to draw the liquid through the foam. Thicker foams created more nucleation sites and greater heat transfer area, but if too thick, the vapor release resistance would dominate and decrease the heat transfer performance. The foams with low pores per inch (ppi) values (30 and 60) had higher maximum heat transfer coefficients but the foam with a high ppi value (90) could dissipate higher heat fluxes but had a considerably higher wall temperature.

A wicking structure is interesting in that it can sustain large heat fluxes, although it requires large wall superheats. Mori and Okuyama [30] used a porous, honeycomb plate which was designed for an exhaust gas filter on combustion engines. It was found that the vertical pores in the plate allowed for vapor to move away from the surface while dryout was prevented by the capillary wicking of the material. This structure was able to attain 251 W/cm^2 of heat flux, but at a wall superheat of 50 °C.

Li and Peterson [31] created a copper mesh structure with sintered copper wire screens applied to a copper foil. The 8 mm x 8 mm mesh structure was attached to a larger copper foil and was heated by an 8 mm x 8 mm copper bar. They varied the porosity, pore size and thickness of the structure. They found that thicker foils could reach higher heat fluxes, but thinner structures were more effective with lower superheats. Also, evaluating pore sizes of 119.2 µm, 140 µm, and 232.2µm, the study showed that the smallest pore size was the most effective heat transfer surface.

2.6 Heat Transfer Mechanisms

Throughout the boiling curve, there are several ways heat can be removed through the solid surface to the fluid. Before bubbles nucleate, there is only one mechanism which dominates, which is natural convection. After nucleation begins, other forms of heat transfer come into play. Most notably, due to the energy required for phase change the latent heat required for liquid evaporation is one of the mechanisms. As a bubble grows on the surface, the surrounding liquid is pushed away from the bubble, thereby introducing microconvective currents. Due to the difference in the wall temperature and bulk liquid temperature, the fluid

motion along the heated surface allows for heat transfer. After a bubble departs from the heated surface some of the bulk liquid replaces the space evacuated by the bubble. As the temperature of this liquid rises to reform the thermal boundary layer, this form of heat transfer is known as transient conduction.

One of the earliest studies to find the importance of the various mechanisms in nucleate boiling was by Judd and Hwang [32]. In their study, dichloromethane was boiled on a glass surface and visualized using a high speed camera. By measuring the volume of the microlayer evaporated, they attributed microlayer evaporation to be responsible for a third of the total heat transfer. They were able to develop a correlation which could sum together the heat transfer effects of the microlayer evaporation, natural convection and nucleate boiling (microconvective) effects.

More recently, Moghaddam and Kiger [33] boiled FC-72 on a silicon substrate with temperature sensors embedded into it. Using temperature and high speed video data, they were able to detect temperature changes as the bubble formed and departed. The data showed decreases in temperature as the bubble interface crosses the sensors, showing that the bubble ebullition cycle yields heat transfer. The authors determined that the microlayer evaporation had the smallest contribution to total heat transfer with transient conduction having the highest and microconvection having a high contribution at high surface temperatures.

2.7 Critical Heat Flux

Many researchers have disputed the root mechanism for the CHF. Some researchers have explained the CHF as instability due to different fluid properties between the liquid and

vapor interface. Zuber [34] suggested that in the microlayer, Taylor and Helmholtz instabilities would result in a dryout scenario. Other researchers also explained the CHF condition through hydrodynamic instabilities, such as Haramura and Katto [35] and Moissis and Berenson [36].

Fundamental to the boiling process are the forces and characteristics of bubble generation. Kandlikar [37] conducted a force balance on a bubble to predict CHF. He found that the forces involved are due to evaporation momentum, surface tension and gravity. A nondimensionalized form of the CHF quantity was related to other nondimensional quantities such as Weber number, Capillary number and the ratio of evaporation momentum force to surface tension force in the correlation.

2.8 Nucleate Boiling

For bubble nucleation to occur, a heated surface must attain a temperature higher than the saturation temperature. As many researchers have noted, roughness in the form of creating cavities can augment the degree of superheat required for nucleation to occur. These cavities and in particular, reentrant cavities can entrain vapor under the heated surface. This allows for the cavity to be active, and subsequently capable of bubble generation.

Kandlikar and Spiesman [38] nondimensionalized the nucleation criterion produced by Hsu [7] so it could be applied to a wide range of fluids resulting in the following forms:

$$r^* = r / \delta_t \tag{2.1}$$

$$\Delta T_{sat}^* = \frac{\Delta T_{sat} h_{lv} \delta_t}{8 \sigma T_{sat} v_{lv}} \tag{2.2}$$

$$\Delta T_{sub}^{*} = \frac{\Delta T_{sub} h_{lv} \delta_t}{8 \sigma T_{sat} v_{lv}} \tag{2.3}$$

The range for active cavities for a given nondimensional superheat and subcooling is bounded by the maximum and minimum cavity radii:

$$r_{\max}^{*}, r_{\min}^{*} = \frac{1}{2}\left[\frac{\Delta T_{sat}^{*}}{\Delta T_{sat}^{*} + \Delta T_{sub}^{*}} \pm \sqrt{\left(\frac{\Delta T_{sat}^{*}}{\Delta T_{sat}^{*} + \Delta T_{sub}^{*}} \right)^2 - \frac{1}{\Delta T_{sat}^{*} + \Delta T_{sub}^{*}}} \right] \tag{2.4}$$

Equation 2.4 shows that there exists a single point, where the maximum and minimum cavity radii are equal, that there is a critical cavity radius. When the term under the square root of Equation 4 is zero, nucleation occurs at the lowest possible wall superheat.

2.9 Scope of Work

In general, heat transfer enhancement seen in the literature is directed to generating bubble nucleation. By increasing the nucleation site density, more bubble growth occurs which increases the amount of heat dissipation. However, more vapor on the surface risks dryout so this does not always increase the CHF, and often it will decrease the CHF value.

This study aims to look at the physical mechanisms behind the bubble dynamics and heat transfer. Using open microchannels, surfaces will provide locations where bubbles can nucleate and grow. High speed video will be used to image the bubble dynamics, in an effort to better understand how the growth and movement of bubbles can contribute to heat transfer, through various means. Quantitative measurements for heat flux and surface temperature will be used to compare the performances of different surfaces for the different microchannel geometries.

3. Experimental Setup

The test section consists of the test chip, with a water reservoir above it and a heated copper block below it. The copper block is heated with a cartridge heater, while the water reservoir has an auxiliary heater to keep the liquid at the saturation temperature.

To apply a heat flux to the test section, a 450 W capacity cartridge heater was inserted into a copper block to serve as the heating element. The copper block was machined to have a 1 mm x 1 mm tip which was 25 mm long. Three K-type thermocouples, starting 3 mm from the tip of the block and each spaced 8 mm apart from each other and were used to measure the temperature gradient through the tip of the copper block. The heat flux was then calculated as:

$$q'' = -k_{Cu}\frac{dT}{dx} \tag{3.1}$$

The temperature gradient, $\frac{\mathrm{dT}}{\mathrm{dx}}$ was calculated using a three-point backward space Taylor Series approximation, assuming no side losses:

$$\frac{\mathrm{dT}}{\mathrm{dx}} = \frac{3T_1 - 4T_2 + T_3}{2\Delta x} \tag{3.2}$$

At the top of the boiling pool, a 100W auxiliary heater was used to keep the water at the saturation point. A fourth thermocouple is placed in the water reservoir to measure the bulk water temperature, ensuring that the tests are conducted at saturation temperature. An NI-cDaq-9172 data acquisition system was used in conjunction with a NI-9213 card to record

the temperatures during testing. A LabVIEW virtual instrument (VI) was also created to display temperatures, determine when the system was at steady-state, and record the data.

A schematic of the test section design is shown in Fig. 3.1. A Keyence® high speed digital camera was used to image the boiling phenomena an angle of 15°. The camera was inclined at this angle so that nucleation at the heated surface was properly imaged. The high speed color camera has frame rates capable of 24,000 frames per second. In order to keep resolution satisfactory, the frame rates used were 1000 frames per second.

For the tests, a layer of conductive, polysynthetic silver thermal paste was used to decrease the contact resistance between the copper block and silicon chip. Screws with springs underneath the caps were placed on both sides of the chip, and were compressed to a length of 6 mm, for the same amount of force applied between the chip and the copper block for each test. Contact resistance was quantified, as discussed in a later section.

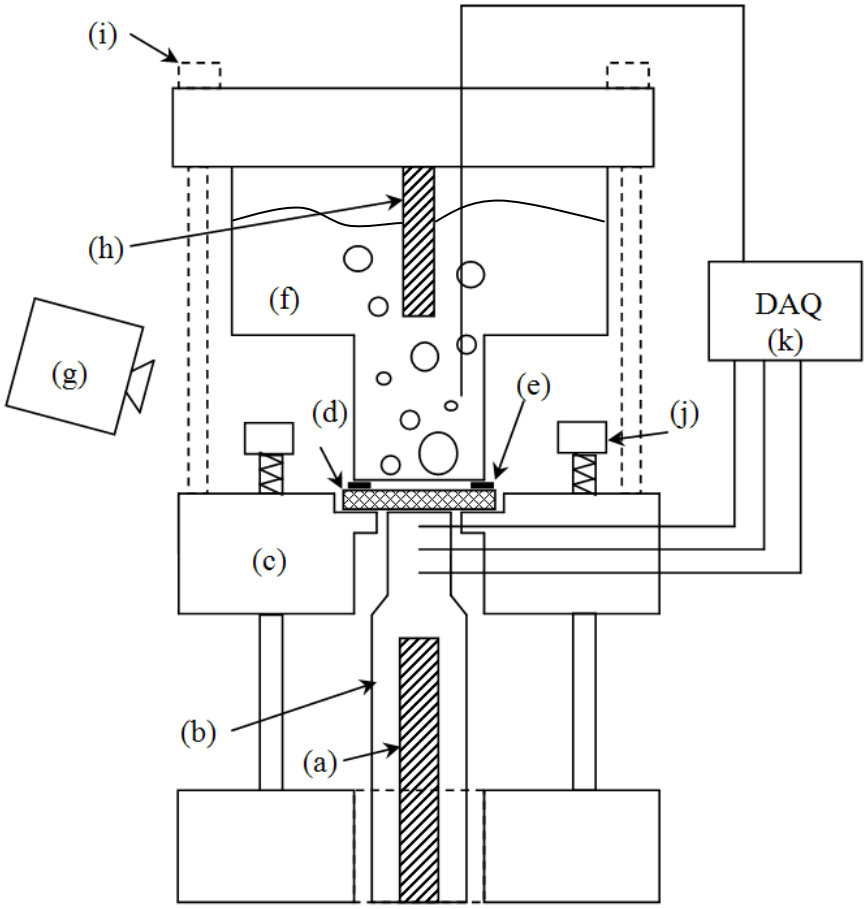

Figure 3.1. Schematic of boiling test fixture (a) cartridge heater (b) copper heating block (c) insulating block (d) silicon test chip (e) gasket (f) polycarbonate visualization tube (g) high speed camera (h) auxiliary heater (i) compression screws (j) compression screws (k) data acquisition with 4 K-type thermocouples

For every test, distilled water was used to ensure it was free from contaminants. Water is chosen because of its well known fluid properties, and minimal risk handling the fluid, compared to a refrigerant. The water is allowed to be boiled sufficiently in order to reduce the effects of any dissolved air within the fluid. Periodically during the tests, more water is added to the pool to replenish the evaporated water vapor. The water is allowed to reach steady-state before any data is collected.

3.1 Setup Calibration

A two-point thermocouple calibration was done primarily to have the thermocouples read accurately and secondly to determine the precision and bias of the thermocouples. The bias and precision errors of the thermocouples were used in the uncertainty analysis of the system, described in a later section.

Thermal contact resistance was a factor in the test setup. Due to small asperities between the copper heating block and the silicon chip, a layer of thermal paste was applied to decrease the contact resistance. To ensure that the pressure between the surfaces was constant for each test run, compression screws with springs were used to provide the same amount of force between the test chip and the heating block.

In order to quantify the contact resistance of the test fixture, a 3 mm thick copper chip was created, with a thermocouple hole located 1 mm from the end. A schematic of the contact resistance measurement along with an equivalent thermal circuit are shown in Fig. 3.2. A square channel was machined into the copper chip, around the area of the heater, to ensure that the heat transfer remained one dimensional.

Sandwiched between the copper chip and the copper block is a silicon chip of the same area as the heater. This layer helps to provide the same conditions for the contact as in actual testing: a copper-thermal paste-silicon combination. Inserting two layers of thermal paste (one on each side of the silicon) allows for a more accurate measurement of the contact resistance because it is averaged between the two sides.

Tests were conducted from a high heat flux of about 120 W/cm^2 and power was gradually reduced, taking steady-state data points at various heat fluxes. Then the heat flux

was then increased, with data recorded at steady-state values. The contact resistance was calculated using Eq. 5.1:

$$R''_{t,c} = \frac{1}{2}\left(\frac{T_1 - T_4}{q''} - \left.\frac{L}{k}\right|_{Cu,1} - \left.\frac{L}{k}\right|_{Si} - \left.\frac{L}{k}\right|_{Cu,2} \right) \tag{3.3}$$

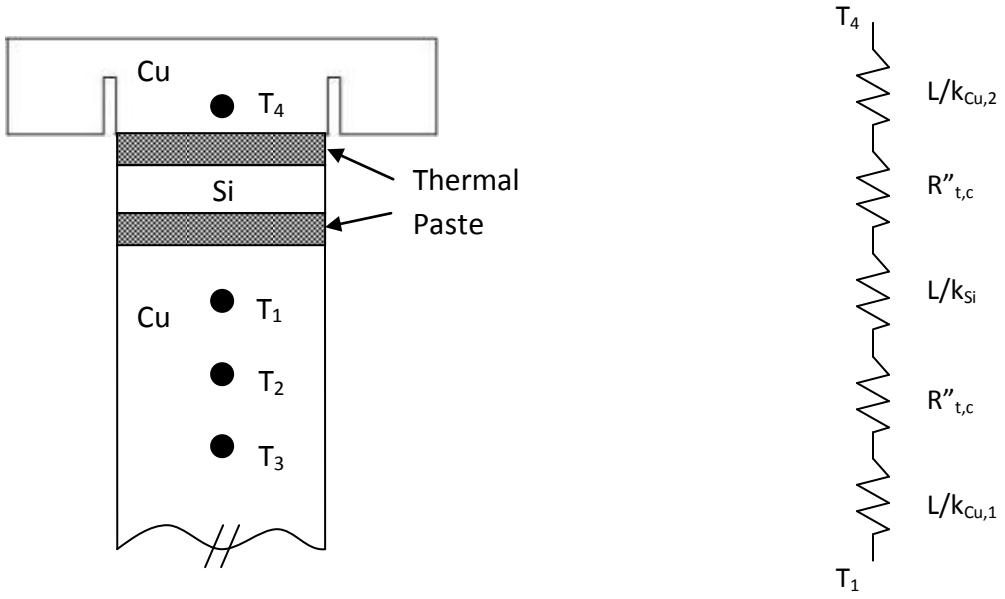

(a) (b)

Figure 3.2. (a) Schematic of copper chip setup for contact resistance calculations (not to scale) (b) equivalent thermal circuit for 1-D heat conduction analysis

The contact resistance was consistently found to be 5 x 10^{-6} m^2K/W, with an uncertainty of less than 4 percent. Using this contact resistance, the surface temperature of a test chip can be calculated using the heat flux through the copper block, as well as the thermocouple T_1 from the following relation:

$$T_s = T_1 - q''\left(\frac{L_{Cu}}{k_{Cu}} + R''_{t,c} + \frac{L_{Si}}{k_{Si}} \right) \tag{3.4}$$

3.2 Uncertainty Analysis

Experimental uncertainty is inherently in all analyses, and can best be divided into two groups of error: bias and precision. Bias, or systematic errors occur repeatedly with each measurement. These are typically due to calibration, loading or resolution. Precision errors are more random, due to fluctuations or low sensitivity in testing equipment that can be determined through a statistical analysis. The error of a physical quantity can be expressed as the square root of the sum of the squares of the bias and precision errors.

$$U_y = \sqrt{B_y^2 + P_y^2} \tag{3.5}$$

In this study, there are three categories of parameters where uncertainty can originate. The first is from the thermocouples calibration accuracy and precision resolution. Each thermocouple has a specific precision, which has been determined through a statistical analysis. This was determined during calibration at a steady-state temperature, finding twice the standard deviation of the average reading to obtain a 95% confidence interval for the precision error. Another source of uncertainty is from the thermal conductivity of materials changing under temperature changes. The value is found in lookup tables, but with the system under various temperatures, there will be some variation in the true value of the property. The uncertainty of the thermal conductivities of copper and silicon for the range of operating temperatures are 2.2% and 3.7%, respectively. The uncertainty for length measurements, the spacing between thermocouples and thicknesses of materials were determined by the resolution of the equipment used to measure the distances. The uncertainty values for the parameters used in the study are shown in Table 3.1.

Table 3.1. Uncertainty parameters

Parameter	Value	Units	U_p	Value	% Uncertainty
k_{Cu}	401	W/m-K	$U_{k,Cu}$	9	2.2
k_{Si}	100	W/m-K	$U_{k,Si}$	3.7	3.7
L_{Cu}	0.003	m	$U_{L,Cu}$	0.00025	8.3
L_{Si}	0.000725	m	$U_{L,Si}$	0.000025	3.4
$R_{t,c}$	5.00×10^{-6}	m^2-K/W	$U_{R,t,c}$	5.00×10^{-7}	10
Δx	0.008	m	$U_{\Delta x}$	0.0001	1.3
T_1	Varies	°C	U_{T1}	0.11	N/A
T_2	Varies	°C	U_{T2}	0.075	N/A
T_3	Varies	°C	U_{T3}	0.075	N/A

With care in an experimental setup, the uncertainty of any given parameter may be small (< 5%), but using multiple parameters in equations can propagate the uncertainty. When using a formula to evaluate a parameter, i.e. heat flux or surface temperature, the uncertainties in the components used in the calculation can add up to influence that parameter. From Eq. 3.1, the error in the heat flux, *q"* of the system is affected by the errors of the thermocouples, the thermal conductivity of the copper block, as well as the spacing between the thermocouples. The method used to find the error propagation is through partial sums, expressed in Eq. 3.6.

$$U_p = \sqrt{\sum_{i=1}^{n} \left(\frac{\partial p}{\partial a_i} u_{a_i} \right)^2} \tag{3.6}$$

where p is the calculated parameter, a_i is a measured parameter, and u denotes the uncertainty of the subscripted parameter.

The uncertainty for the heat flux can be derived from Eqns. 3.1 and 3.2 by using the partial sums described in Eq. 3.6. Dividing by the heat flux value yields the uncertainty as a percentage of the calculated value. This final expression is shown in Eqn. 3.7:

$$\frac{U_{q''}}{q''} = \left[\left(\frac{U_k}{k} \right)^2 + \left(\frac{3U_{T_1} \cdot k_{Si}}{\Delta x \cdot q''} \right)^2 + \left(\frac{4U_{T_2} \cdot k_{Si}}{\Delta x \cdot q''} \right)^2 + \left(\frac{U_{T_3} \cdot k_{Si}}{\Delta x \cdot q''} \right)^2 + \left(\frac{U_{\Delta x}}{\Delta x} \right)^2 \right]^{1/2} \tag{3.7}$$

The surface temperature uncertainty can be found in the same manner using the partial sums from Eq. 3.4. Dividing by the calculated surface temperature, the percent uncertainty is calculated by Eq. 3.8:

$$\frac{U_{T_s}}{T_s} = \left[\begin{array}{l} \left(\frac{U_{T_1}}{T_1 - q'' R_{tot}} \right)^2 + \left(\frac{U_{q''}}{\frac{T_1}{R_{tot}} - q''} \right)^2 + \left(\frac{U_{L_{Si}}}{\frac{k_{Si} T_1}{q''} - k_{Si} R_{tot}} \right)^2 + \left(\frac{U_{k_{Si}}}{\frac{k_{Si}^2 T_1}{q'' L_{Si}} - \frac{k_{Si}^2}{L_{Si}} R_{tot}} \right)^2 \\ + \left(\frac{U_{L_{Cu}}}{\frac{k_{Cu} T_1}{q''} - k_{Cu} R_{tot}} \right)^2 + \left(\frac{U_{k_{Cu}}}{\frac{k_{Cu}^2 T_1}{q'' L_{Cu}} - \frac{k_{Cu}^2}{L_{Cu}} R_{tot}} \right)^2 + \left(\frac{U_{R''_{t,c}}}{\frac{T_1}{q''} - R_{tot}} \right)^2 \end{array} \right]^{1/2} \tag{3.8}$$

$$R_{tot} = \left(\frac{L_{Si}}{k_{Si}} + R''_{t,c} + \frac{L_{Cu}}{k_{Cu}} \right) \tag{3.9}$$

The sum of the resistances in the calculation is represented as R_{tot}, expressed in Eq. 3.9. After calculating the uncertainties for heat flux, the uncertainty increases from 2 x 10^4 W/m^2 to 6 x 10^4 W/m^2 from the low to high heat fluxes. However, at low heat fluxes this value comprises 20% of the calculated value, but at the high heat fluxes it is only slightly more than 4%. This is considered to be acceptable because chip performance is evaluated at elevated heat fluxes.

The uncertainty of the surface temperature was calculated to be between 4.5% and 4.6% throughout the range of heat fluxes.

3.3 Heat Loss Study

In order to ensure that the heat generated from the cartridge heater and moving through the copper tip was transferred to the pool of water for boiling, a heat loss study was conducted. The copper tip is insulated on its sides with fiberglass insulation in order to reduce the heat lost. A steady, one-dimensional heat conduction temperature profile should be linear, as described by Fourier's Law. Figure 3.3 shows a typical temperature profile along the copper tip during a test. The figure shows the temperature profile to be approximately linear along the length of the copper tip. The heat flux is proportional to the thermal gradient and $\frac{dT}{dx}$ is a constant at any point along the copper; therefore there is no heat loss along the length of the copper tip.

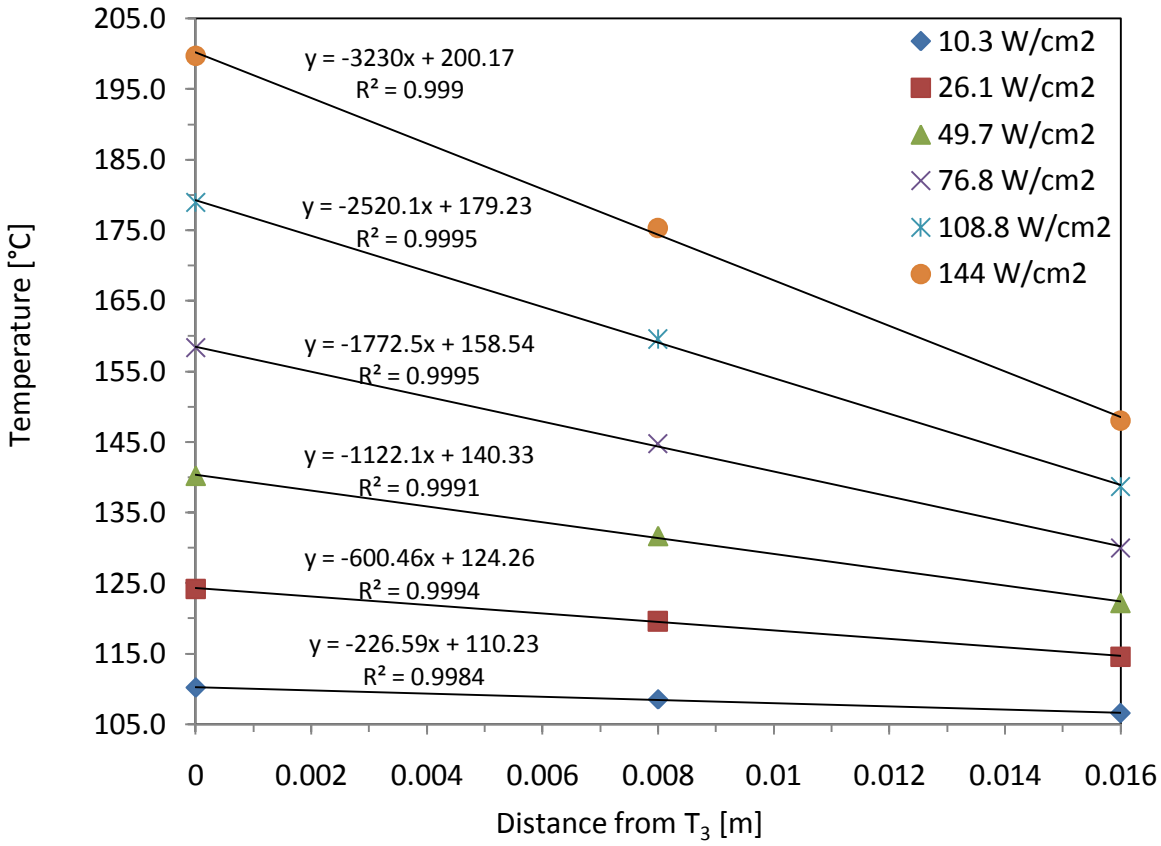

Figure 3.3. Temperature measurements along copper tip for thermocouples 1, 2, and 3 for various heat fluxes

In order to investigate the possibility for heat to be lost to the ambient air through natural convection due to the upper portion of the test fixture, the heat loss study was continued. The water in the visualization tube was replaced with fiberglass insulation to eliminate natural convection off of the chip surface. A small amount of power was applied to the cartridge heater and after the system reached steady state, the temperatures through the copper tip were recorded.

The characteristic temperature needed to quantify the power loss was the surface temperature, T_s. This was calculated from Eq. 3.4. This was used to find the differential temperature, which is the ambient temperature subtracted from the surface temperature.

$$\Delta T_{amb} = T_s - T_{amb} \tag{3.10}$$

The heat measured through the copper tip at a particular differential temperature is the amount of heat loss from the test section. The relationship between heat loss and differential temperature is shown in Fig. 3.4. As the trend shows, the heat loss is a linear function of the differential temperature.

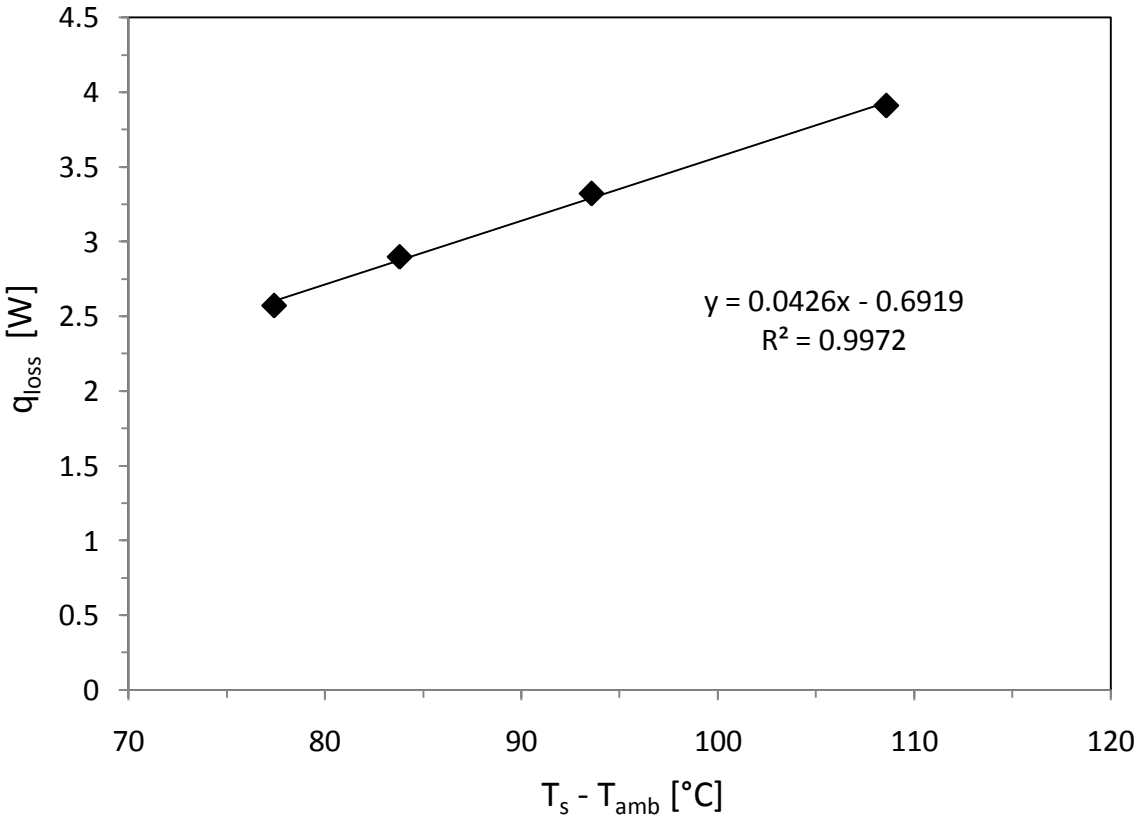

Figure 3.4. Heat Loss for a given differential temperature, measured for the PTFE block with silicon chip

Using the relationship between heat loss and differential temperature, the heat flux can be calculated taking into account the loss in heat flux. The heat loss is normalized by the area of the copper tip.

$$q''_{corrected} = q_{measured}''-\left(0.0426 \cdot \Delta T_{amb} - 0.6919\right) \cdot 10^4$$

(3.11)

Since the heat loss occurs after reaching the chip, the heat flux is the same throughout the copper tip and across the thermal paste. Therefore, in order to calculate the corrected surface temperature the heat flux changes across the thermal resistance for conduction for the chip. Eq. 3.12 expresses the correction for the surface temperature.

$$T_{s,corrected} = T_1 - q_{measured}''\left(\frac{L_{Cu}}{k_{Cu}} + R''_{t,c}\right) - q''_{corrected}\left(\frac{L_{Si}}{k_{Si}}\right) \tag{3.12}$$

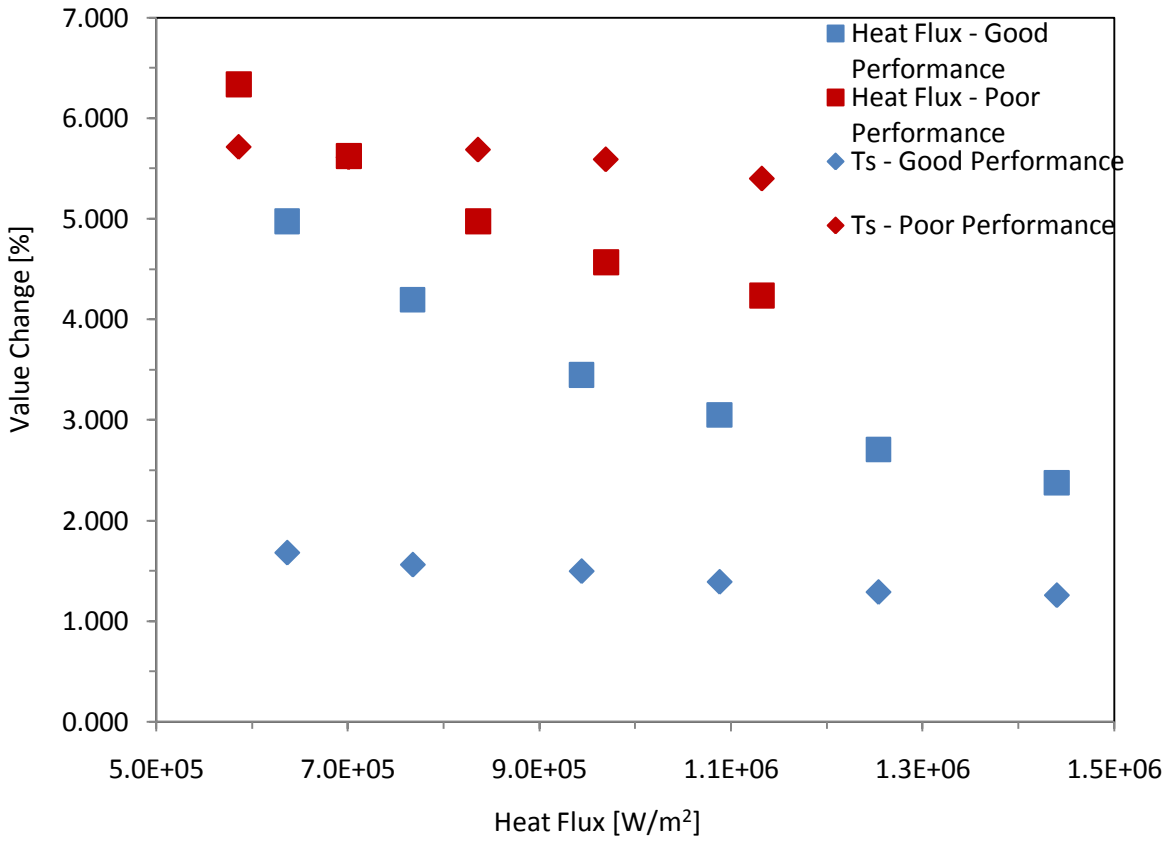

Figure 3.5. Value change in percentage for heat flux and surface temperature when accounting for heat loss

To find out the percentage difference between the original heat flux or surface temperature and the value when taking into account the heat loss, Eq. 3.13 is used.

$$\%\ \ Difference = \frac{|original - corrected|}{original} \cdot 100 \tag{3.13}$$

Figure 3.5 shows the value change for multiple heat fluxes for two test cases: a chip with high heat transfer performance (chip D) and a chip with poor heat transfer performance (chip A). The details of the chips will be discussed in a later section. The heat fluxes during nucleate boiling show that the value change is low – about 5% for the two chips. For the chip with greater heat transfer enhancement, this value change is much lower than the uncertainty calculated in Section 4.2, while the chip with a poor heat transfer performance has a value change that is close to the calculated uncertainty. Since the percent change is less than or equal to the uncertainty, the heat loss can be ignored in the preliminary study.

3.4 Data Acquisition

To log data, a LabVIEW virtual instrument (VI) was created. The key data that needed to be recorded were the temperatures of the thermocouples. The sampling rate was set to 4 samples/sec, in order to be have an appropriate response time for an ungrounded, exposed thermocouple. The thermocouples, four for the silicon study and five for the copper chip study were recorded to a spreadsheet, and from the spreadsheet the heat flux and surface temperature were calculated. Figure 3.6 shows a screen shot of the LabVIEW VI.

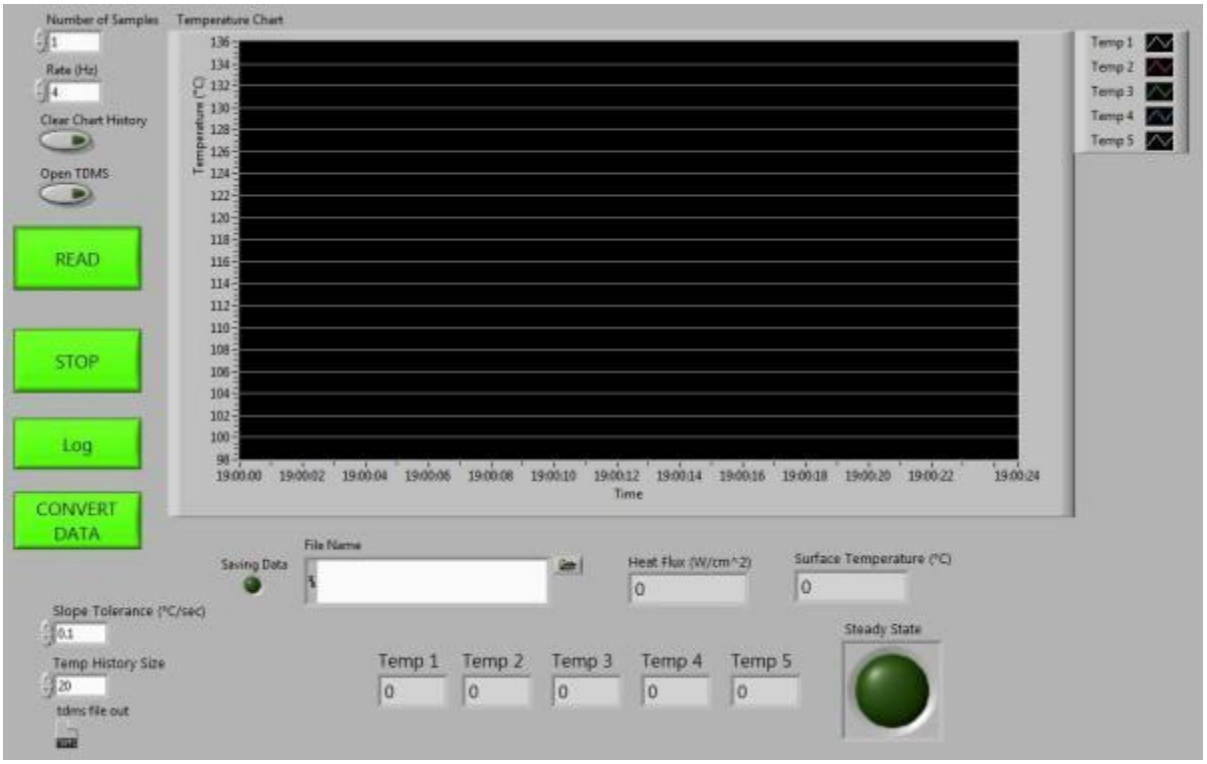

Figure 3.6. LabVIEW virtual instrument

All data was recorded at steady state, and to quantify that steady state had been reached an indicator was integrated into the VI. This indicator, in the form of a light, turns on when all thermocouples are only varying by the standard noise, determined as twice the standard deviation from the calibration. Over a course of 12.5 seconds, if the thermocouples do not show an increase or decrease by more than the normal noise, the light will turn on indicating the system has reached steady state.

3.5 Setup Repeatability and Validation

A plain silicon chip has been tested repeatedly to ensure the test fixture will produce the same result after numerous runs. The results for four separate tests are shown in Fig. 3.7.

Slight deviations occur for the curves at higher surface temperatures, but the data still remains close together.

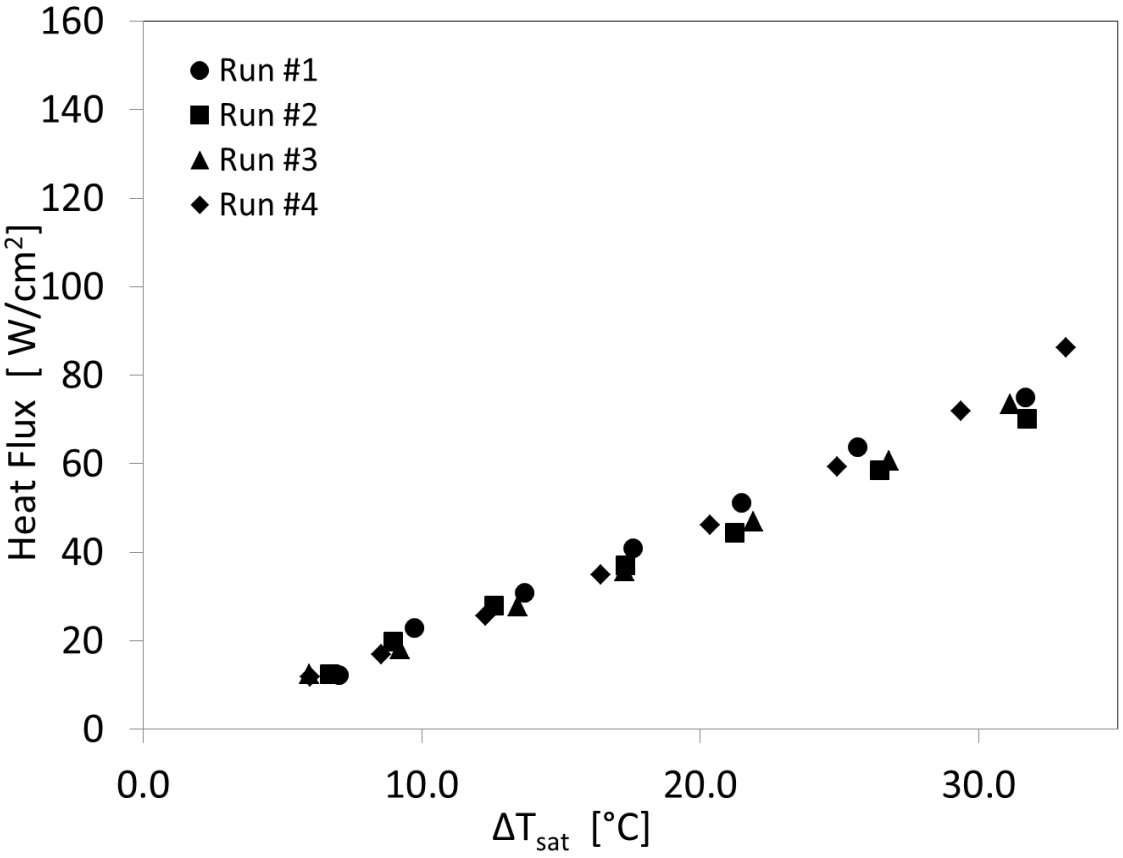

Figure 3.7. Boiling curves for plain silicon chip for four test runs

The boiling curves have also been compared to the plain surface data in literature. Figs. 3.8(a) and (b) show the comparison for silicon and copper, respectively. The plain silicon curves show the plain chip for this study, labeled as Chip A, as well as two other studies in literature. The figure shows that the plain chip data falls between the two data sets from literature. Figure 3.8(b) shows the copper chip data. The plain copper chip has a boiling curve that shows an early onset of nucleation, and has higher heat transfer than the plain surfaces for most surface temperatures. The chip used for this study has an average

roughness value of 0.38 µm, which could be the contributing factor to the higher heat transfer coefficients.

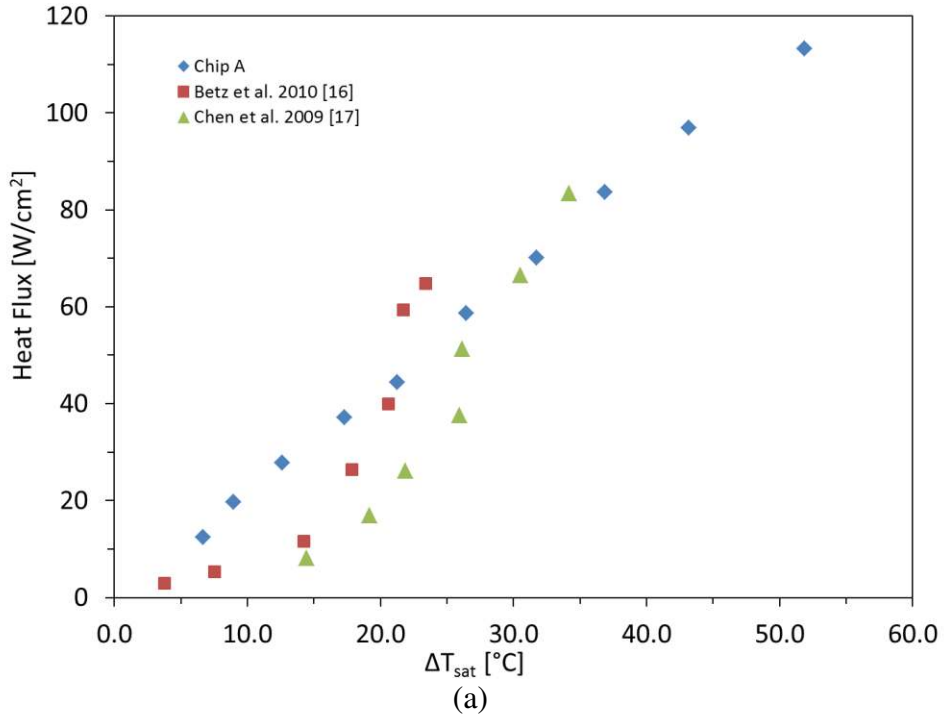

(a)

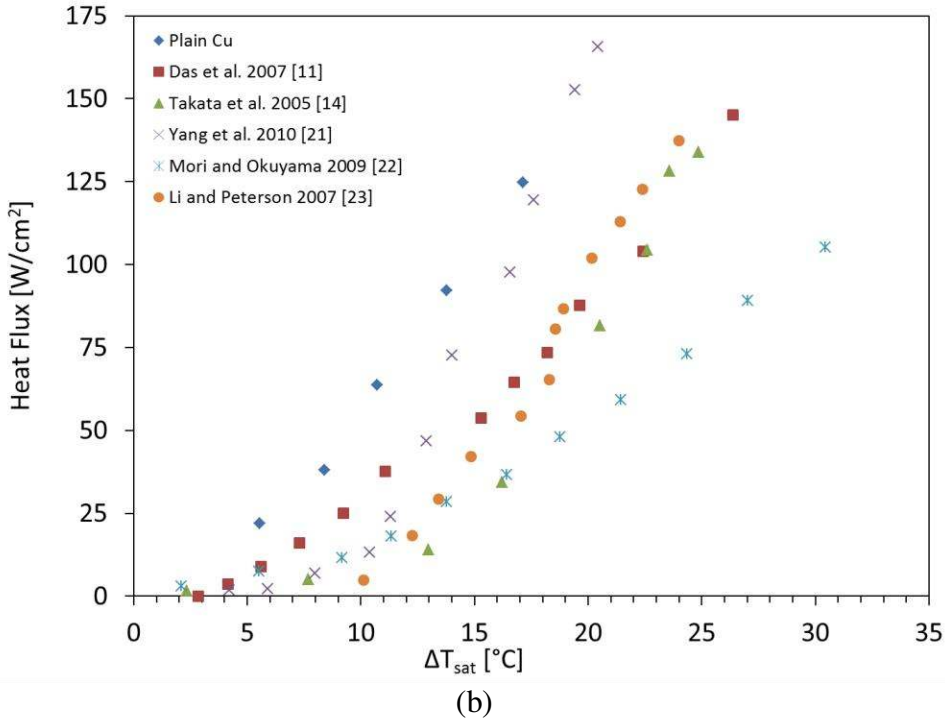

(b)

Figure 3.8. Plain surface data for (a) silicon and (b) copper compared to data from literature

4. Pool Boiling Study with Silicon Chips

4.1 Test Chips

A study has been conducted for silicon chips with surface enhancements. The purpose of this study is to determine the effects of various microstructures than can be etched onto a silicon chip. Table 4.1 describes the five chips that were tested using the pool boiling test fixture, with an example of a chip in Fig. 4.1. The figure shows the heated area, in a dashed red rectangle, where the microstructures are located. Each chip has overall dimensions of 2 cm x 2 cm, with the heated micromachined area of 1 cm x 1 cm. These chips, used in a previous study, have been fabricated by the IBM T.J. Watson Research Center using a deep reactive ion etching method (DRIE). This technique has become a common method of micromachining silicon wafers, and is effective at removing areas off the surface of the silicon, while retaining near vertical sidewalls.

Table 4.1. Silicon chips tested for preliminary results

Name	Type	Groove (μm)	Fin (μm)	Depth (μm)	Notch	Surf. Area Increase
A	Plain	N/A	N/A	0	No	1.000
B	Microgroove	200	200	208	No	1.916
C	Microgroove	200	200	192	Yes	1.996
D	Microgroove	100	100	275	Yes	3.745
E	Microgroove	100	100	182	Yes	2.817
F	OSF (500 μm long, 1600 fins)	40	60	180	No	3.922

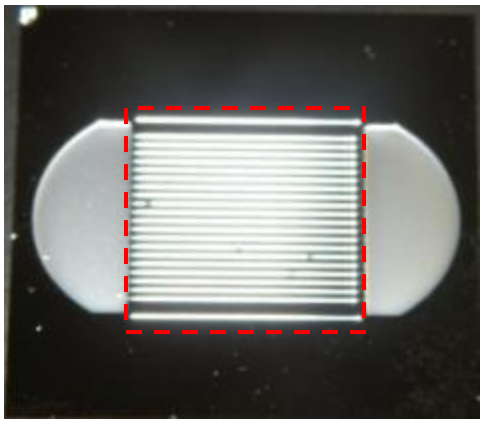

Figure 4.1. Sample silicon chip with heated area outlined in red

In this study, 5 different categories of etched chips were used. A plain surface, three different microgrooves and an offset strip fin (OSF) design were used for boiling testing and visualization. One of the microgroove designs is repeated; chip D has the same microgroove design as chip E, but with a substantially deeper etch depth. This selection of chip designs has been used to evaluate the effects of microgrooves and fins during the boiling process, as well as evaluating the effects of cavities incorporated into the chip design.

Using a Keyence® laser confocal microscope, chip dimensions and parameters were quantified. The average roughness of the plain chip was determined to have a *Ra* value of 0.030 µm. Chips that have been DRIE etched have an *Ra* value of 0.470 µm on the bottom surface.

Figure 4.2 shows the detail of the chips, Fig. 4.2(a) for the plain chip, Fig. 4.2(b) for chip B, Fig. 4.2(c) for chip C, Fig. 4.2(d) for chips D and E, and Fig. 4.2(e) for chip F. Figures 4.2(c) and 4.2(d) show that for chips C, D, and E, there is a rectangular notch along the walls of the microgroove spaced every 100 µm. These are vertical notched tunnels on the sidewalls of the channels. Each of these cavities is 10 µm wide by 20 µm deep into the channel wall. It was postulated that providing the fluid with a location, surrounded by walls on three sides would enhance the heat transfer by providing possible nucleation sites. This

would allow for a large number of effective sites, allowing for several active sites during the boiling process. As part of an earlier study using similar chips, an SEM image from Steinke and Kandlikar [1] is shown in Fig. 4.2(f), showing that although the channels were designed to be rectangular, the etching process produced channels more trapezoidal in shape. Actual channel dimensions for each chip are listed in Table 4.1.

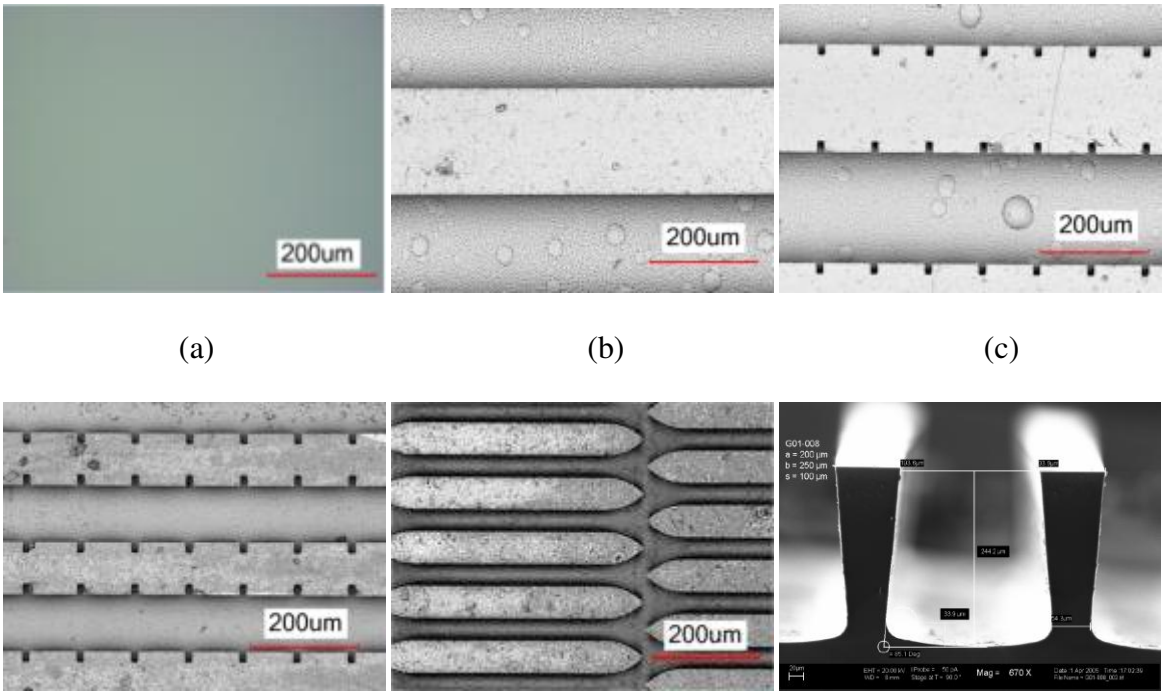

Figure 4.2. (a) – (e) Surface images of chips used at 20x magnification (f) example of a 250 µm deep channel cross section taken from [1]

4.2 Silicon Chip Results

Figure 4.3 shows the results of the boiling tests for each chip. The results shown are from the data points in which the power was increased. The data with decreasing power do not show any hysteresis effects, and follow the increasing curves very closely.

The figure shows that there is an enhancement when using any chip that has been etched. All of the chips show an increase in performance compared to the plain chip, A. The OSF chip enhances the heat transfer, but not as much as either of the 200 μm channel chips, with the 100 μm channel chip performing the best. Interesting to note is the lack of any improvement with the introduction of the nucleation sites, which is seen with the 200 μm channels.

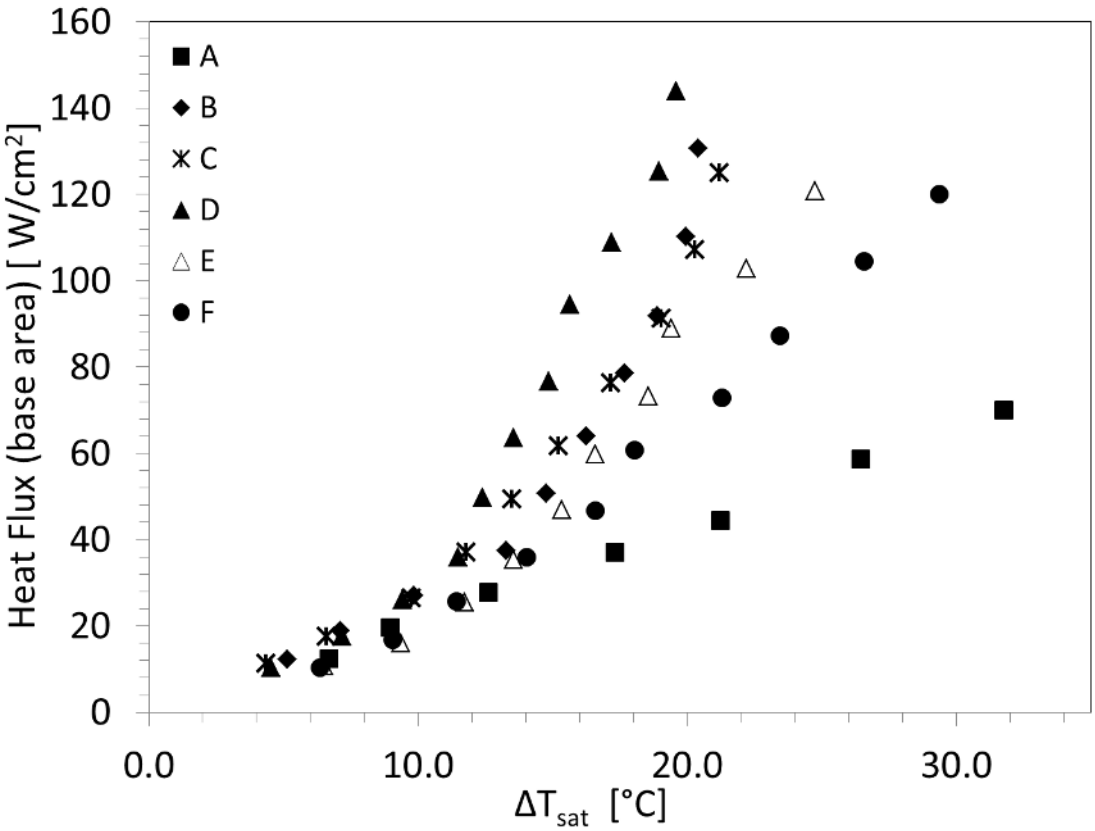

Figure 4.3. Boiling curves for each of the chips tested based on projected heater area

It is clear from Fig. 4.3 that more heat can be dissipated through the etched chips (B-F) compared to the plain (chip A) for the same wall superheat. However, there may be two reasons for this enhancement: (i) the increased surface area of the etched chips allows for more heat transfer, area and (ii) the structure of the chips affects the mechanics of pool boiling through interface motion within the microstructures.

For each of the different chips, there are different boiling curves. However, it is difficult to discern whether the enhancement is due to the added amount of surface area that is produced after the surface modification. The increase in area for the etched surfaces promotes an increase in heat transfer because it allows for more convection from solid to liquid as well as providing an increase in the number of possible nucleation sites. Therefore it is beneficial to evaluate the surfaces for the heat flux applied to the chips, but normalized to reflect the area over which the fluid contacts the surface. Using this parameter, the surfaces can be compared by the surface geometries, rather than the solely the increase in area.

Figure 4.4 shows the boiling curve for the chips, with the heat transfer normalized with respect to the wetted surface area of the heated surface. Since there are no enhancements to the plain chip, A, the curve remains unchanged. For the etched chips, the curves are shifted lower by the ratio of the base area to the wetted surface area. At low superheats, all of the etched chips performances fall below the plain chip. At higher wall superheats the 200 μm wide microgroove chips B and C show improvement over the plain chip. By the nature of the curve, it appears that at higher heat fluxes, chip D would follow the same path. However, it is not clear that chip E would perform better than the plain chip at higher values. Chip F, with the substantial increase in surface area with 1600 fins, the heat flux for a given wall superheat is always lower than the plain chip.

Comparing the data from Figs. 4.3 and 4.4, it is clear that the increase in surface area has some effect on why the etched chips show enhancement in heat transfer. For chips E and F, an increase in heat transfer is due solely to the increase in area. For chips B and C, the increase in area is responsible for the enhancement at low wall superheats. At the higher wall superheats, there is an increased heat transfer performance, despite normalizing the area. This means that there is an enhancement mechanism at work, with the geometry of the etch having an effect. Chip B has slightly better improvement over chip C, which shows that the increase in area in the rectangular etched sites along the channel walls do not have any significant effect. Increasing channel and fin sizes shows an increase in heat transfer for the chip, despite having only a slight increase in surface area of the chip.

Comparing the data between chips D and E, with similar geometries, chip D can dissipate more heat for a given wall superheat. This is attributed to the depth of etch on each of the surfaces. Applying heat to the bottom surface of the chip, the chip with the deeper etch will have a greater temperature at the floor of the microgroove. In this way, the required superheat for bubble nucleation will be met first with chip D, allowing for a greater amount of active nucleation sites. Due to the increase in activation sites, there will be an increase in heat transfer for the chip, due to the associated latent heat flux.

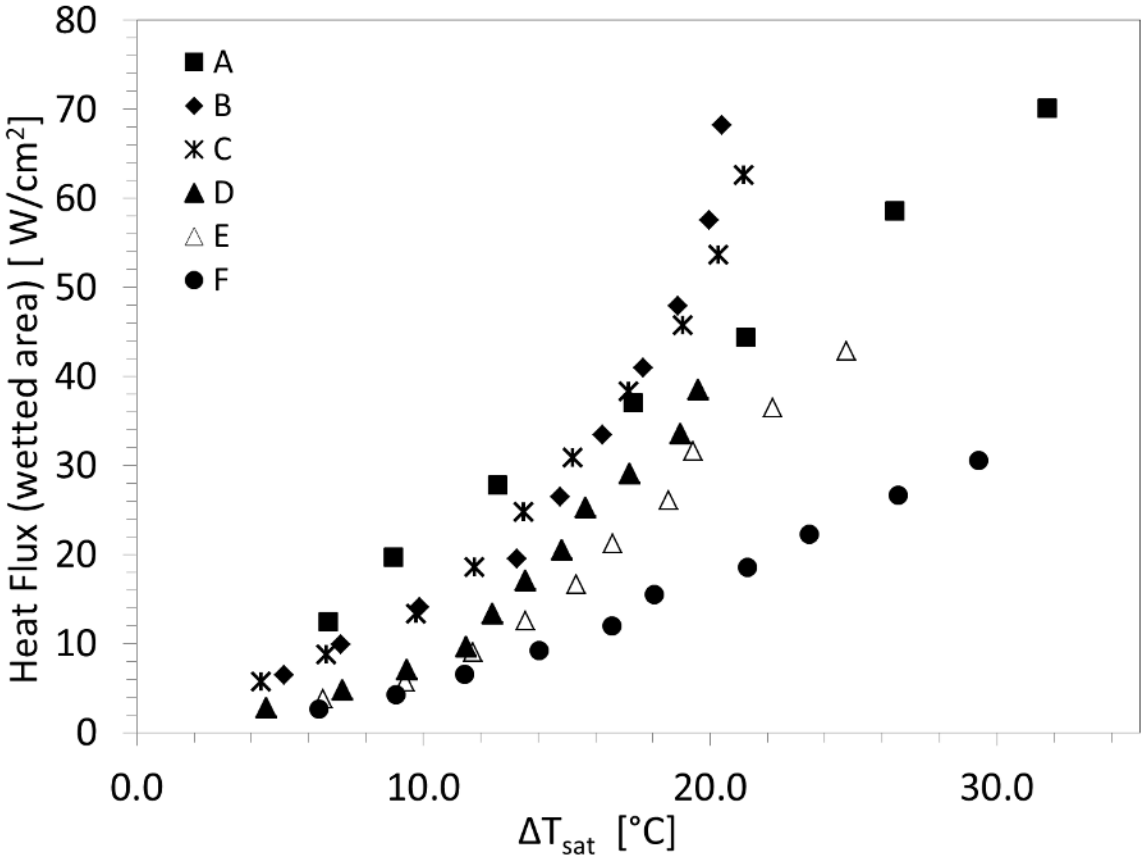

Figure 4.4. Boiling curve for the chips tested with the heat flux normalized to the wetted surface area

The bubble nucleation and growth in microgroove surface were investigated with high speed camera. Figure 4.5 shows a nucleation event on chip C at a low heat flux of 18 W/cm^2, with images on the left and a representation of the image on the right. The depictions on the right show an enlarged nucleating bubble for clarity. In Figure 4.5(a) the white arrow points to a bright point on the bottom surface of the microgroove. This point is a small vapor bubble. After the bubble reaches the top of the channel in Fig. 4.5(c), it experiences rapid growth on top of the land between the two microgrooves Fig. 4.5(d). The bubble then departs off the surface after it has grown to a considerable size.

The motion of the bubble is remarkable in that it moves from a location at the bottom of the microgroove to the top of the fin where it attaches itself to the surface and then grows. It is not known whether it moves vertically up the channel wall or up within one of the nucleation sites. Since the base of the microgroove is closer to the source of the heater, there would be a greater temperature at the base than at the top, even if that difference is small. Also, the etched section of the chips has a roughness that is greater than the portions that have not been etched to provide more nucleation sites. The individual frames of the other videos show the nucleation activity similarly. If it were necessary for this small bubble to have a cavity to grow to considerable size and depart, the etched bottom of the microgroove would is more favorable.

The individual frames of other the videos show the nucleation activity similarly. Bubbles have rapid growth at the top of the microgrooves. Videos show that there is water flooding the channel. If indeed all bubbles on these surfaces nucleate in this way, liquid dryout of the surface would only pertain to the tops of the walls, leaving evenly distributed dry and flooded areas. This may decrease the amount of localized hot spots, which occur under vapor bubbles on the surface. Also, this provides two different areas that are influenced by the bubble activity.

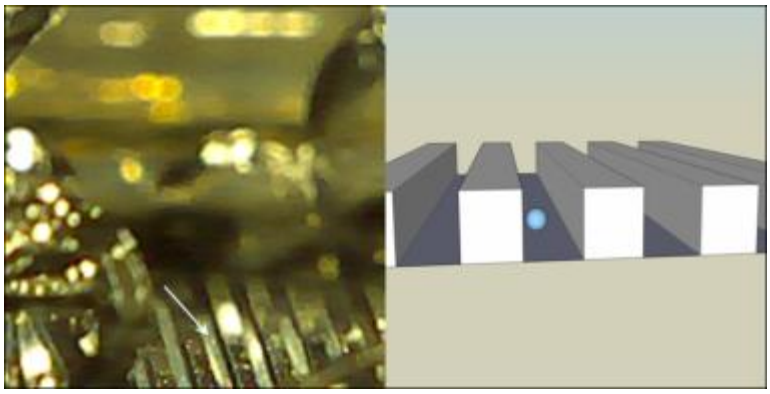

(a) time = 0 ms: nucleation on the bottom surface

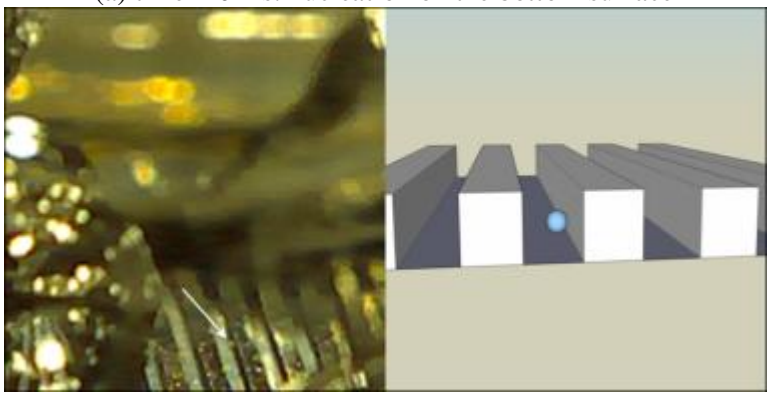

(b) time = 2 ms: bubble movement to channel sidewall

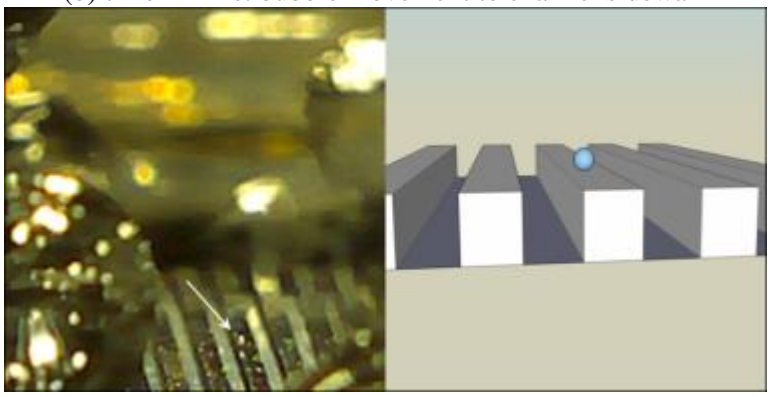

(c) time = 5 ms: bubble movement to the top wall of channel

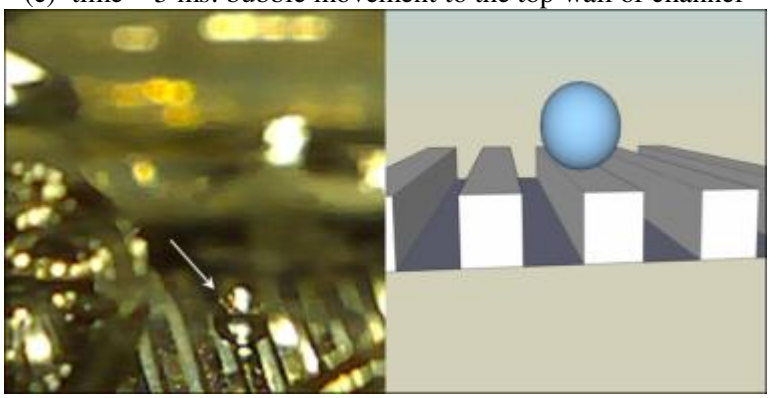

(d) time = 8 ms: bubble growth on the top wall of channel

Figure 4.5. Successive images of bubble nucleation on chip C at 1 ms intervals

Figure 4.6 shows the boiling sequence of bubble growth on chips B and F at heat fluxes of 97 W/cm^2 and 93 W/cm^2, respectively. At these higher heat fluxes, much vapor is generated at the top of the fin surface leaving the microgrooves open to liquid supply. For the chip with microgrooves etched onto the surface, the areas in which the fluid evaporates remains relatively in the same place. However, chip F has moving vapor fronts. Similar events have been noted by other researchers [39], although only for smooth surfaces. This is equivalent to periods of evaporation, followed by periods of the fluid rewetting the surface. This trend is not seen at lower heat fluxes in which the boiling regime is characterized by isolated bubbles. When there are isolated bubbles, there is a substantially longer waiting period for nucleation, and it decreases as the heat flux is increased. At high heat fluxes, there is much more vapor generated. Chips A and F experience the vapor generation, with nucleation occurring at various active sites. For the chips with microgrooves, B, C, and D, the microgrooves provide efficient pathways for the water to reach the nucleation sites for evaporation, without the vapor becoming detached from the heated surface. This allows for consistent boiling, with little waiting time between successive bubbles.

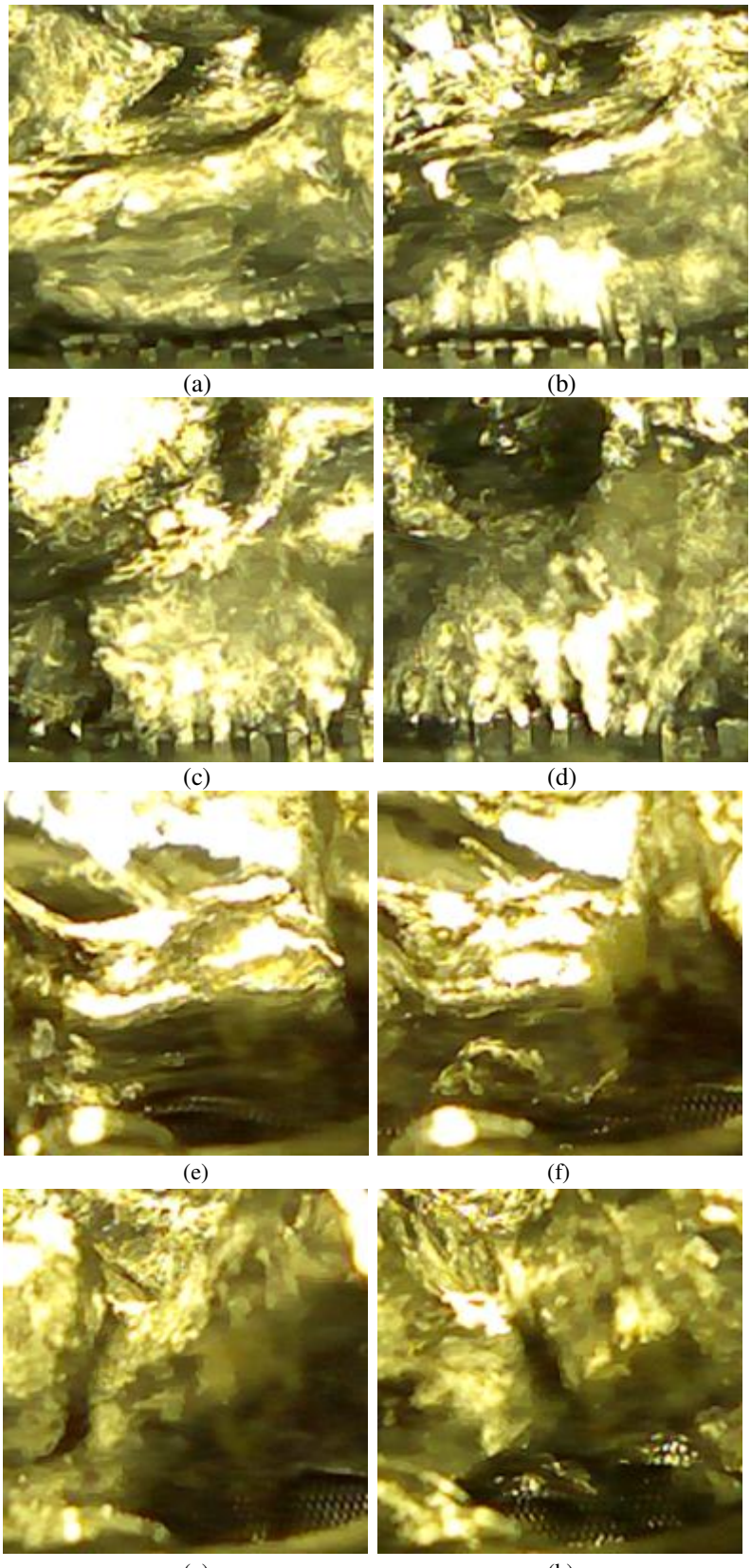

Figure 4.6. Successive images at 2 ms intervals of high heat flux boiling for chips B (a - d) and E (e - h)

4.3 Heat Transfer Mechanism

Based on the high speed video observations from Figs. 4.5 and 4.6 as well as heat transfer data from Figs. 4.3 and 4.4, the mechanism responsible for this improvement in heat dissipation by the silicon chip can be postulated. Fig. 4.3 shows that an enhanced surface has the ability to augment the boiling curve from the plain chip. Etched surfaces and in particular deep etched surfaces can improve the heat transfer capabilities. A carefully chosen geometry can further improve the boiling curve, so that the enhancement is not achieved by merely the increase in area, but by a hydrodynamic mechanism.

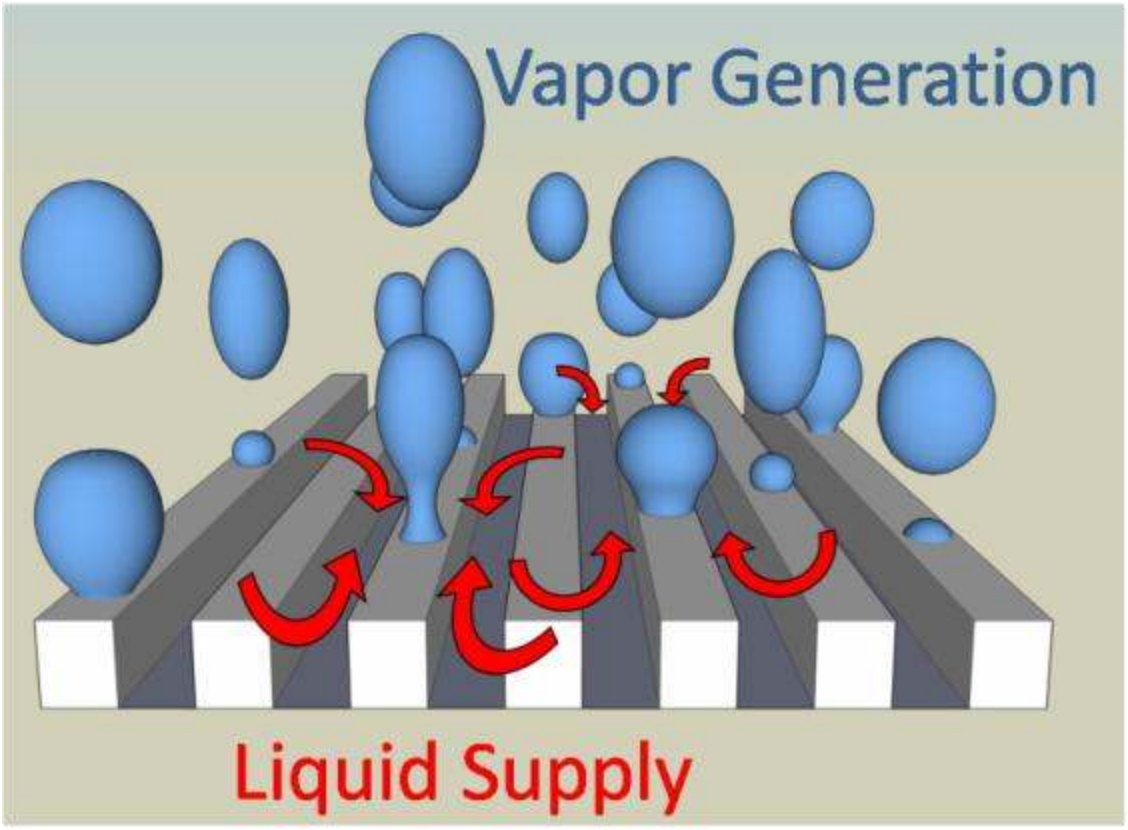

Figure 4.7. Proposed mechanism of bubble dynamics on a microgroove surface (not to scale)

Figure 4.7 shows the schematic of the vapor generation and liquid transport mechanism on a heated surface with microgrooves, with several nucleation sites. As shown in Fig. 4.5, the majority of bubble growth does not occur within the channel. The bubbles grow after they become attached on the top surface of the microgroove walls. Due to the structure of the microgrooves beneath it, large amounts of vapor generation do not dry out the channels. Instead, the channels remain flooded, which provide pathways for the water. With water in the channels, a supply of liquid is brought to the nucleation sites and liquid is evaporated at the liquid-vapor interface. This does not allow for an excessive localized wall superheat because most of the heated area is in contact with the liquid. The liquid flow within the microgrooves results in a very high heat transfer coefficient due to the small hydraulic diameter of the passages. This mechanism in reducing the wall superheat along with the efficient water pathways available in microgroove passages helps to stave off the CHF condition and serves as an efficient nucleate boiling surface. This description also explains why the offset strip fin geometry did not perform as well. Due to the configuration of the fins the movement of liquid throughout the microstructure was impeded and hindered performance.

5. Pool Boiling Study with Copper Chips

5.1 Objective of the Copper Chip Study

The purpose of the second investigation involving copper chips was to expand upon the results of the silicon chip study. The extension of the work has been focused on determining which microchanneled geometries provide the most heat transfer. The chips have been tested beyond the thermal limits that were possible with the first investigation, through upgrades to the test fixture materials.

5.2 Upgraded Test Fixture

An upgraded test fixture was fabricated in order to withstand the elevated temperatures that occur for high heat dissipation and in the event of the CHF condition, seen for the plain chip. In the silicon chip test fixture, the major limitation was the thermal limit of PTFE, the material used as an insulating block which supports the chip. This block is represented as item (c) in Fig. 3.1. After CHF is reached, the heat flux decreases as the surface temperature rapidly increases. Since the melting point of PTFE is around 175 °C, a more suitable material was selected. The new material selected for the test setup is an alumina silicate machinable ceramic. The ceramic material is capable of withstanding temperatures up to 593 °C, with actual operating temperatures below the thermal limit.

The other change to the test fixture involves the viewing tube, item (f) in Fig. 3.1. The highest operating temperature for polycarbonate is around 125 °C. This is too low for the

bottom of it to be in close contact with the chip surface. The upper surfaces of it which are exposed to the saturated water are sufficient for use in the upgraded fixture. The lower portions of it will be replaced by four optically clear, fused quartz pieces, assembled together with an acrylic adhesive and sealed with a silicon sealant. The fused quartz windows have a much higher maximum operating temperature than the polycarbonate.

5.3 Test Chips

Copper test chips, similar to the chips used for the contact resistance measurements have been tested with various microchannel geometries machined on the surface. The copper chips have thermocouple measurement capabilities which will eliminate any variation in contact resistance to provide a more accurate value for the surface temperature of the chip. While the first study involved mostly microchannels with equal dimensions for channel width and fin width, these chips use channel and fin widths of different dimensions. Table 5.1 describes the chips that have been tested with the upgraded test setup.

Table 5.1 Copper chip test matrix

Chip #	Groove Width (µm)	Fin Width (µm)	Groove Depth (µm)	# of Channels	Area Increase Factor
1	200	200	208	25	2.06
2	197	200	335	25	2.70
3	197	300	100	20	1.40
4	209	288	115	20	1.46
5	273	224	233	20	1.95
6	295	200	212	20	1.86
7	288	213	445	20	2.83
8	400	200	278	16	1.89
9	375	230	400	16	2.30
10	340	260	380	16	2.22

A representation of the test chips can be shown in Fig. 5.1. It shows Chip #7 – 288 µm channels, 213 µm fins, 445 µm deep. The underside of the chip has a 1 mm channel cut 2 mm deep around the heater area so that the heat will travel one-dimensionally. On the side of the chip there is a hole for a thermocouple to be inserted, which will measure temperature measurements in the center of the chip. On the upper surface are the channels, which will be computer numerical control (CNC) machined.

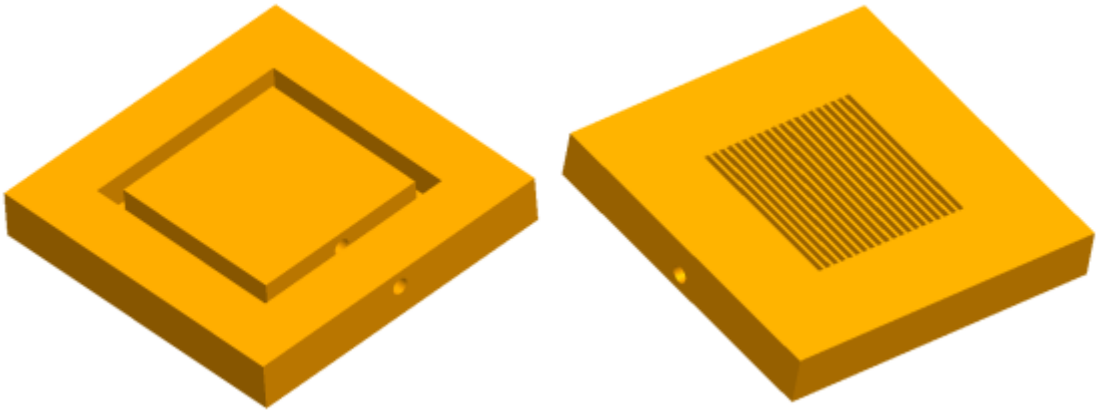

(a) (b)

Figure 5.1. Representations of Chip #7 (a) underside of chip (b) top side of chip

The objective of this study is to evaluate the effect of geometrical parameters of microchanneled surfaces of simulated chips listed in Table 5.1 on heat transfer enhancement during pool boiling with water. These parameters include the channel width, fin thickness and channel depth. An inherent parameter of the chips is the are enhancement factor, which is the ratio of surface area to the projected area of the chip. This wetted area is due to the fin width and channel depth. During the testing of the chips, only the plain chip reached the CHF condition. For all of the other chips, the tests were stopped short because of excessive temperatures within the copper heating block of the test fixture.

5.4 Results

The boiling curves for the tested chips are shown in Fig. 5.2. In this plot, the heat flux has units of W/cm^2 which is common in the electronics industry where 100 W/cm^2 is equivalent to 1 MW/m^2. at the bottom of the microchannels is used in calculating the wall superheat. Expectedly, the plain chip had the poorest performance compared to all the other chips. Conversely, the chip that showed the best heat transfer was chip 9. The boiling curves for the rest of the chips fell in between the plain chip and chip 9. Looking at the geometric parameters of the channeled surfaces, what is most clear is that chips 7, 9 and 10 outperformed the other chips. The commonality between these chips is the width of the channels (more than 300 μm) and the depth of the channels (more than 400 μm). Chip 8 did not perform well, despite having wide channels. This can be attributed to the shallow depth of the channels, at 275 μm.

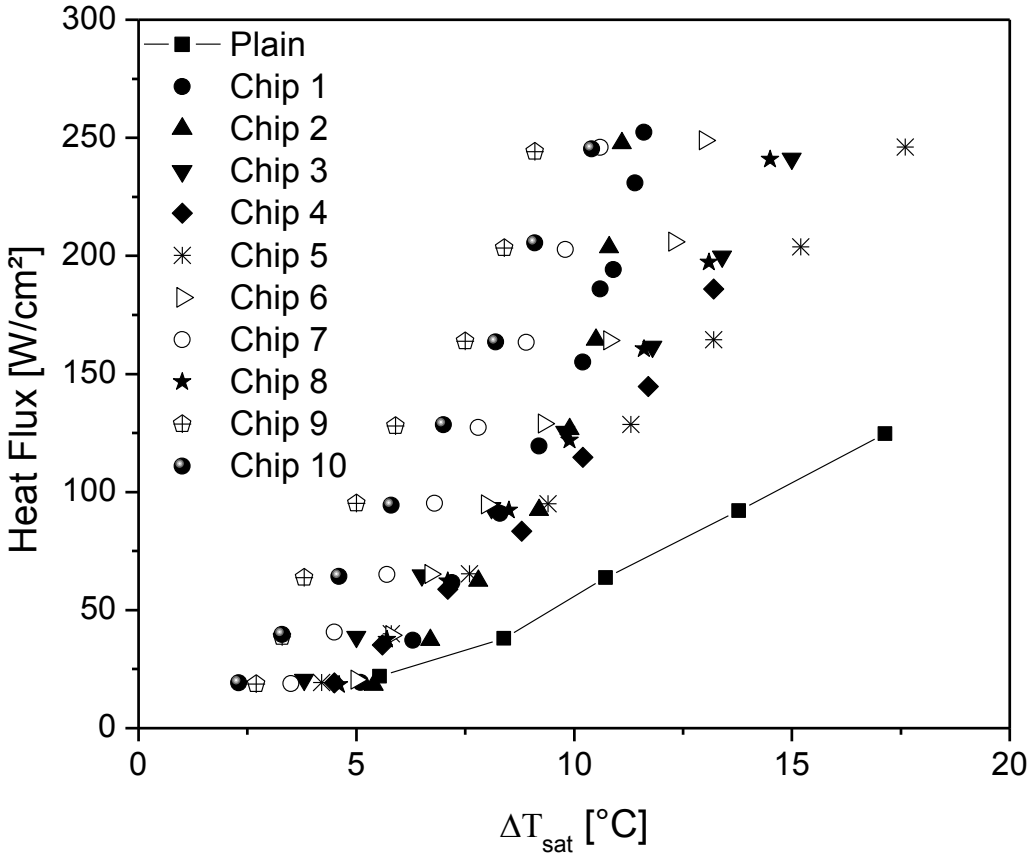

Figure 5.2. Boiling curves for the tested chips based on projected heater surface area

Using the heat transfer coefficient provides a more quantitative way to compare the heat transfer performance. In this study the chips are ranked according to the maximum heat transfer coefficient measured during testing. By plotting the heat transfer coefficient against the wall superheat in Fig. 5.3, the trend shows that as the surface temperature increases, the heat transfer coefficient increases as well for all surfaces. This increase means that the heat flux increases non-linearly with the wall superheat. This is expected because the boiling process enhances heat transfer through the microconvection, microlayer evaporation, and transient conduction mechanisms. As the surface temperature increases, more nucleation sites become active and the nucleation site density increases. The bubble frequency also increases, making the microconvection in the channels more effective. Comparing the best performing

chip to the plain chip, the maximum heat transfer coefficient for chip 9 is 3.7 times that than the plain chip. At the same wall superheat of about 9 °C, chip 9 has a heat transfer coefficient that is over 5 times that of the plain chip.

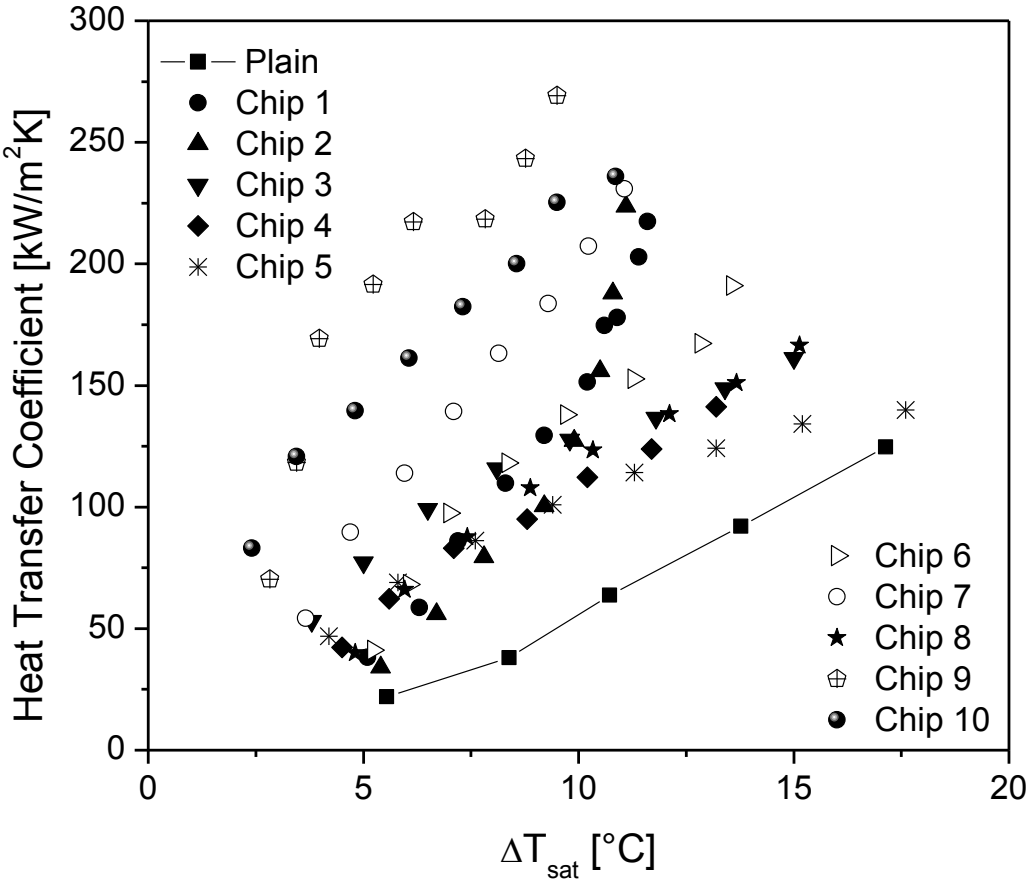

Figure 5.3. Heat transfer coefficients for the tested chips based on projected surface area

5.4.1 Effect of Depth

The depth of the channels is seen to have a significant effect on the heat transfer performance from the chips. From Table 5.1, a few of the chips can be seen to have similar channel widths and fin thickness, but with different depths. These could be compared with chips 5 and 6 versus chip 7, as well as chip 8 versus chips 9 and 10. Figure 5.4 shows there is a trend as the channel depth increases. The data points in the figure represent the heat transfer coefficient when the chips are dissipating 200 W/cm^2 of heat. Chips 5 and 6 have similar

channel dimensions with 7, but chip 7 is more than 200 µm deeper and has a higher heat transfer coefficient. Comparing chips 8 to 9 and 10, the difference in height is over 100 µm, the trend is still true. As the channel depth increases with chips 8, 9, and 10, respectively, the heat transfer coefficient also increases. Although chip 7 has the deepest channels, its performance is not as high as chips 9 and 10 due to narrow channels. This is addressed in section 5.4.2. The effect of deeper channels increasing the heat transfer capabilities of surfaces was also concluded in an earlier work with silicon chips [40].

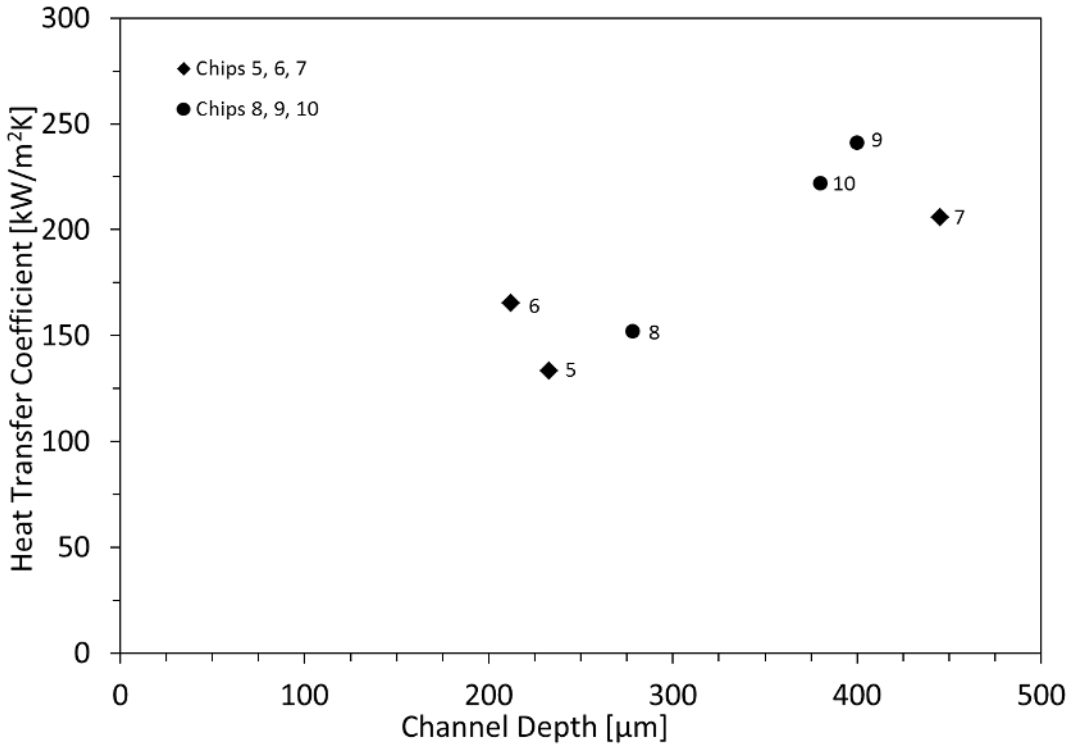

Figure 5.4. Heat transfer coefficient versus channel depth for chips 5 - 10 taken at q"=200 W/cm^2

5.4.2 Effect of Channel Width

The channel width has an effect on the heat transfer performance as well, which is shown in Fig. 5.5. Chips 7 and 9 have a difference of 87 µm in channel width, while other

parameters are quite similar. Although chip 7 has slightly deeper channels, and has more channels for surface area, chip 9 has better performance. Out of the chips tested, ones with the widest channels provide the best heat transfer. Although the best performing chips also have some of the greatest depth, the effect is still present. The role the channel width plays in the mechanism behind the bubble formation and departure is discussed in Section 6.

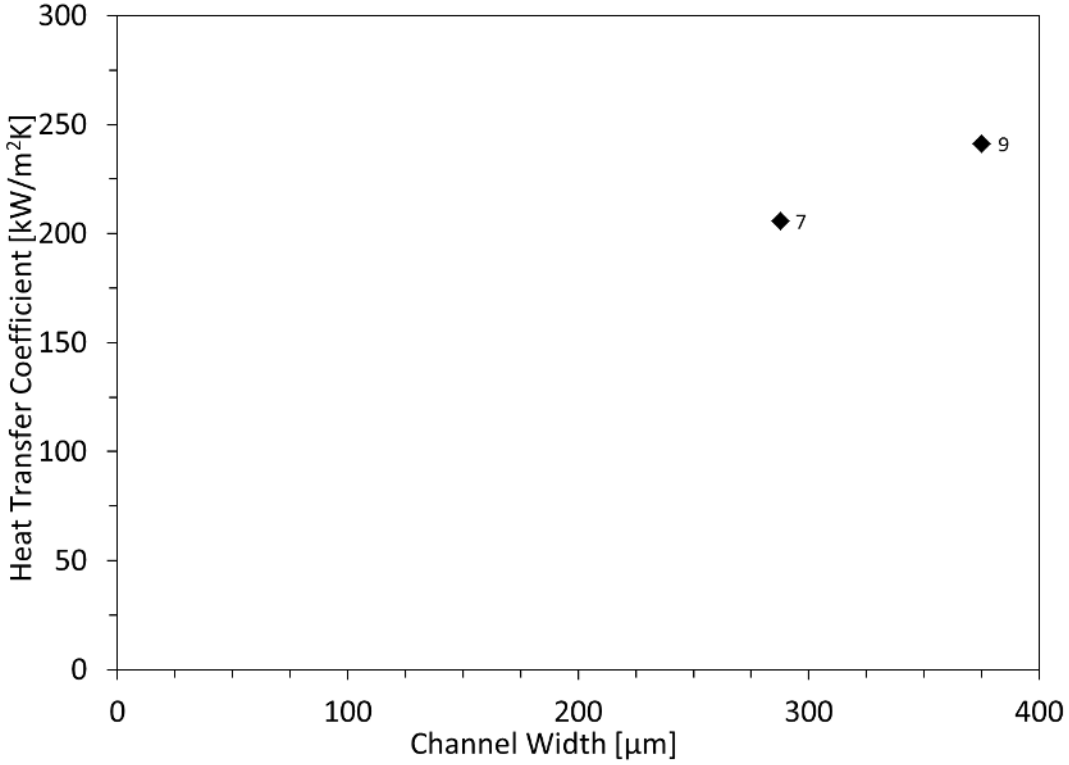

Figure 5.5. Heat transfer coefficient versus channel width for chips 7 and 9 taken at q"=200 W/cm^2

5.4.3 Effect of Fin Thickness

The results from Fig. 5.3 show that the fin thickness has a small effect on the heat transfer abilities of the surfaces. Chip 3, with a fin thickness of 300 µm shows a decrease in performance compared to chip 1 which has a fin thickness of 200 µm. However, some of that heat transfer enhancement could be due to the deeper channel in chip 1 as well. To compare

chips 7 and 10, although chip 7 has thinner fins, the significantly deeper channels of chip 10 dominate the heat transfer.

The depth, channel width and fin thickness all affect the heat transfer performance of a microchanneled chip. The deep channels provide a surface closer to the heater, which will have a higher temperature. This will induce nucleation at lower heat fluxes compared to a more shallow channel or compared to the plain chip. To demonstrate this, a difference of 400 μm at a heat flux of 250 W/cm^2 in copper will produce a temperature difference of 2.5 °C.

However, the fins produced from the channels can act as extended surfaces for heat transfer. For the surfaces, the bottom of the channel will have a higher temperature than the tip of the fin. A fin efficiency analysis has been performed for the chips, using a heat flux of 75 kW/m^{2}K. It was found that for the chips, the fin efficiency ranged between 85% to 97%. This means that there is some, but not a substantial difference in surface temperatures between the bottom surface and the tip of the fin. The fin efficiency was calculated as:

$$\eta_{fin} = \frac{hP}{kA_c} \tag{5.1}$$

Since the fins have more surface area than the bottom of the channel, they will dissipate more heat. As a result of this, the temperature of the channel bottom will be lower than that surface if there were no fins. The fin efficiency analysis can resolve the dependence in temperature of the tip of the fin to the base of the fin, but cannot accurately predict the base temperature. It is suggested that for an accurate depiction of the temperature distribution, 2-D thermal modeling should be done through numerical simulation.

5.4.4 Effect of Surface Area

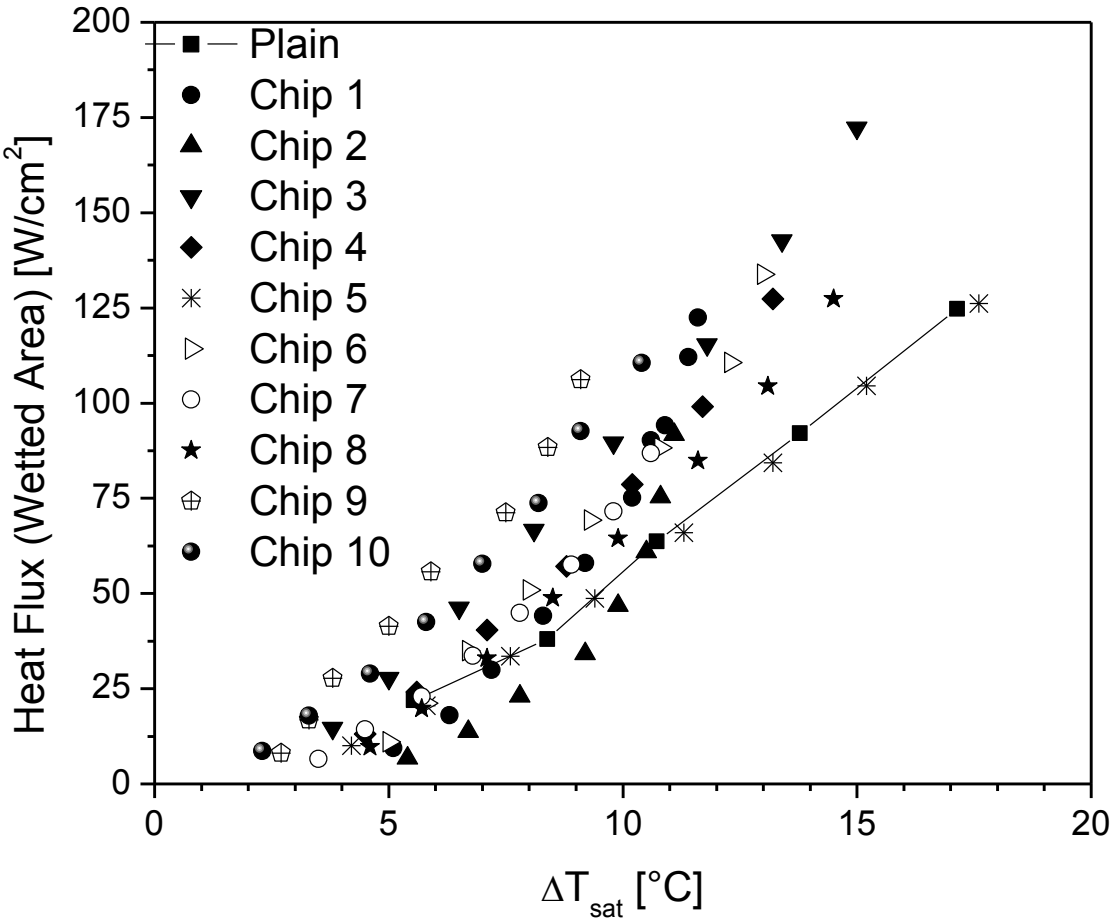

Figure 5.6. Comparison of boiling curves for different chips based on wetted heater surface area

Table 5.1 specifies the surface area increase in the chips due to the presence of microchannels. The factors that affect this area increase are the number of channels and the height of the channel walls. The number of channels are restricted by a 10 mm distance, so the contributing factor is the channel pitch. Chip 2 has the largest area increase because of the small channel pitch, and relatively large channel depth. Chip 4 has the smallest area increase largely due to the shallow channel depth.

Figure 5.6 shows the boiling curves using the actual wetted surface area in the heat flux calculation. The increase in the surface area of all microchanneled surfaces shifts the curves for all them down. Chip 9 is still the best performing chip, with chip 5 the only chip

that falls below the performance of the plain chip (which has no area change). This figure shows that there is a fundamental difference in the heat transfer mechanisms between some of the chips, besides the differences in surface area.

5.5 Comparison to Literature

To get a frame of reference on the performance of the chips from this study, the data are compared with the results from other surfaces reported in the literature. The boiling curves for chip 9, as well as high performing surfaces from 7 other studies are shown in Fig. 5.7. Chip 9 has been plotted using the temperatures at the top of the chip as well as the bottom of the channel, since the data from Das et al. [20] should also be corrected for depth. The curve shifts to the right, but still remains to the left of all the other curves. Other studies have been successful in sustaining large heat fluxes, some above 200 W/cm^2. Using water as the working fluid and a contact angle of 45° (where applicable), the CHF correlations from several authors have been calculated. The correlation Rohsenow and Griffith [41] predict a CHF value of about 135 W/cm^2, while the Kandlikar [42] correlation predicts a value of 127 W/cm^2. Although the correlations are only for a plain surface in pool boiling, the attainable heat fluxes shown by the channeled surfaces show the degree of enhancement. For microchanneled surfaces, the present data, Li and Peterson [31], Takata et al. [24], and Mori and Okuyama [30] all yield much higher heat fluxes. This demonstrates the effectiveness of a microchanneled surface in extending the CHF limit over a plain surface.

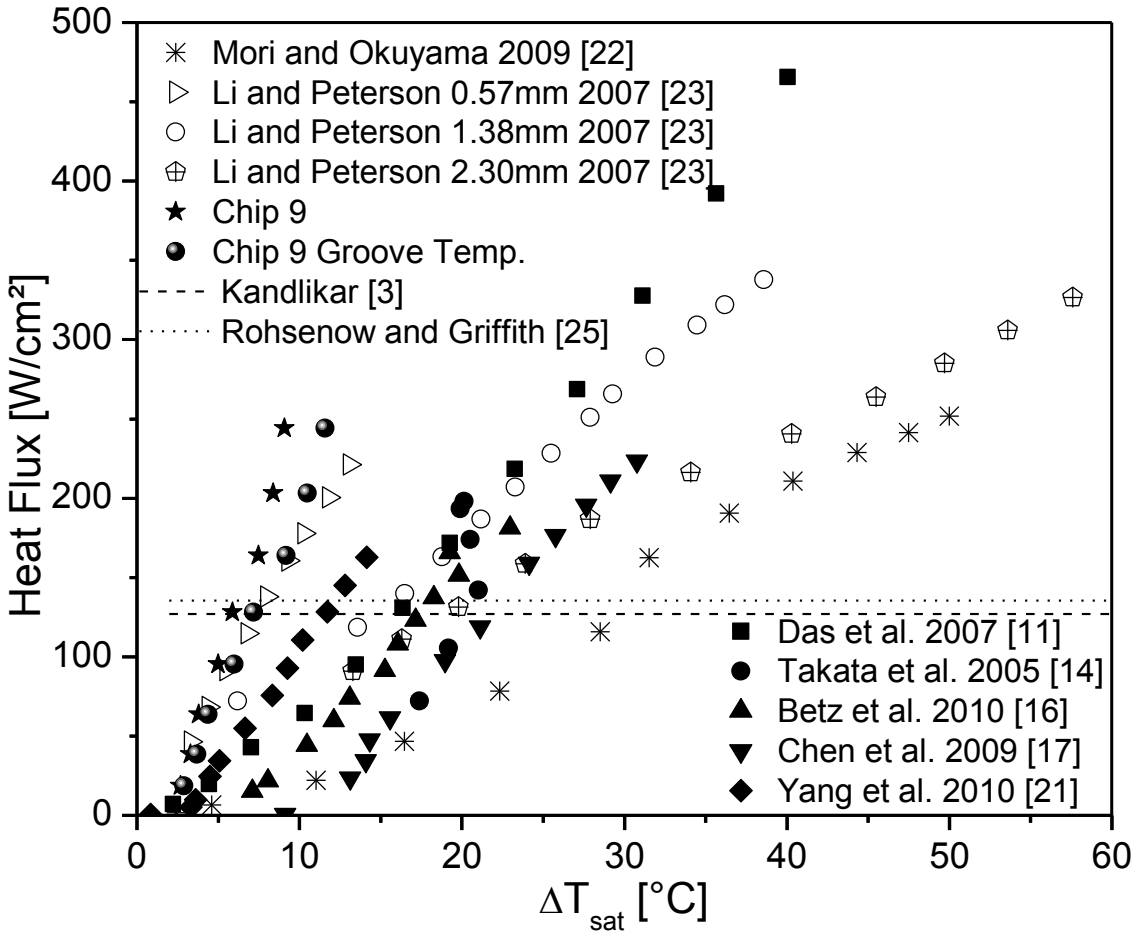

Figure 5.7. Boiling curve comparison for high performing structures in literature

Figure 5.8 shows the heat transfer coefficient for enhanced surfaces in literature at each wall temperature. The performance from the wicking surfaces of Mori and Okuyama [30] and the mesh structures of Li and Peterson [31] do not produce very large heat transfer coefficients. For the data of Li and Peterson [31], the surface that had the best performance was the thinnest mesh structure, with the thick surfaces having relatively constant heat transfer coefficients. This suggests that the thicker structures acted as an extended surface and while water was able to rewet the surface, the amount of vapor generation created some dryout and larger wall superheats.

Chip 9 has outperformed the other available data with a record heat transfer coefficient of 269 kW/m^{2}K. When the wall superheat is taken at the bottom of the channel, the temperature is higher. Even with this correction, the heat transfer coefficient is over 200 kW/m^{2}K, a value which other research studies were not able to reach.

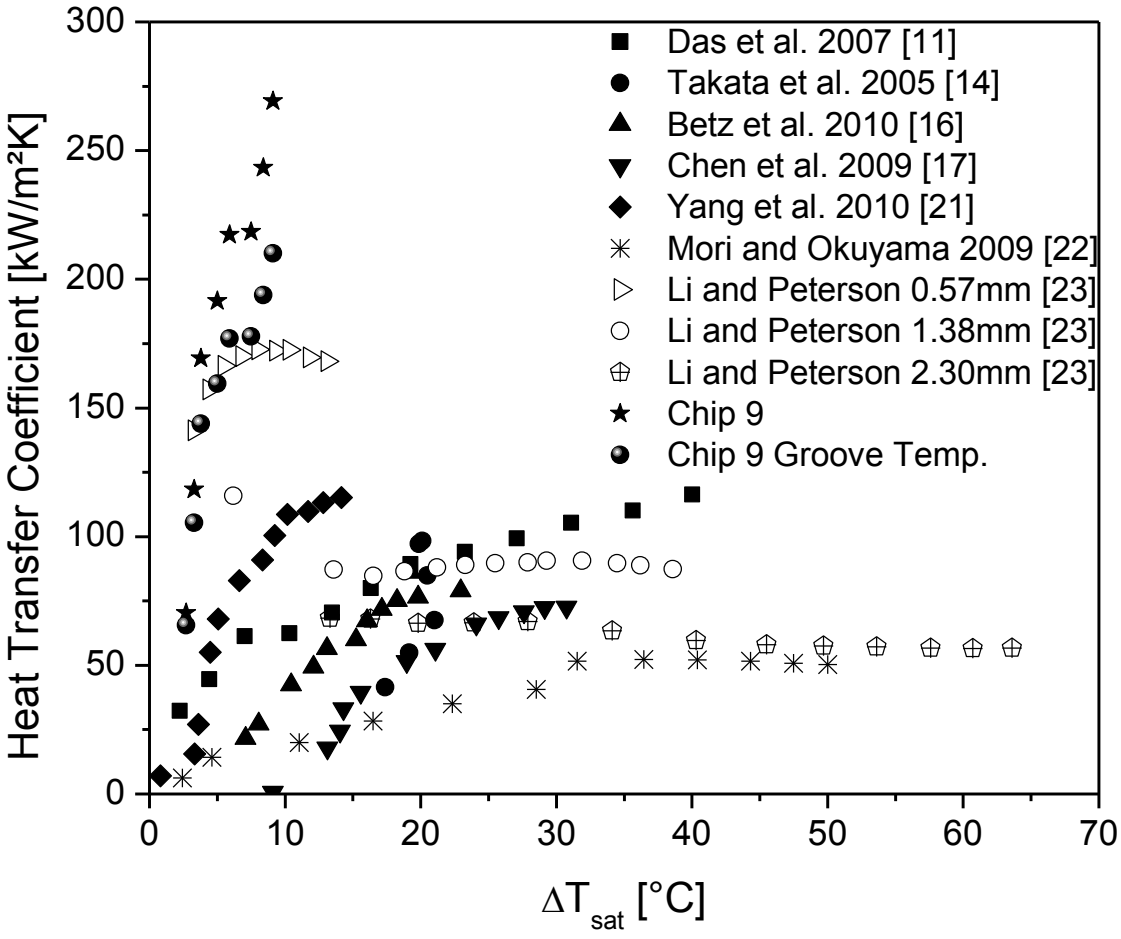

Figure 5.8. Heat transfer coefficient comparison for high performing structures in literature

6. Theory / Mechanisms

For microchanneled surfaces, the surface temperatures were lower as compared to those for a smooth surface at the same heat flux. As described in the earlier publication [40], the microchannels act as conduits for liquid supply to nucleation sites. As the bubbles depart off the surface, the volume that is evacuated by the bubble is replaced by the liquid. This allows for the channels to act as a heated channel with a flow, in which the channel is heated on three sides. In this manner, the advantages in heat transfer to liquid flow can be attained by the large surface area to volume ratio [43].

The high heat transfer abilities of chips 1 and 2 may be due to the small hydraulic diameters of the channels (considering them as channels for liquid flow caused by the interface growth and bubble departure). The other chips with larger hydraulic diameters do not show as much enhancement, except for the chips with very wide channels, which assist in the large amounts of vapor production within the channel itself.

The high speed camera has been used in this study to show bubbles as they nucleate and depart off the surfaces. The camera was only used in low heat flux conditions because at high heat fluxes the boiling process was too rapid and chaotic to image the microchanneled surface. However, the videos that were captured do provide useful insight to the bubble dynamics on two chips.

Figure 6.1 shows a sequence of the high speed images for chip 2 at 2 ms intervals, at a heat flux of 22 W/cm^2. In these images, the microchannels are pointed back into the picture and can be seen. The channels appear darker than the fin lands because of the lack of lighting at the bottom of the channels. At the bottom right of the images are some darker regions,

which are due to the gasket material out of focus and not well lit from the lighting system. To the right and left of the images are vapor bubbles that have been generated both from the heated surface as well as a portion of it could be the result of rogue bubbles from the gasket edge.

What is remarkable of this sequence is how the bubbles are nucleating off the surface. In the video, the small bubble in the center of the image nucleates from the same site while another bubble does the same, two channels to the left of it. The shape of the bubbles is still spherical, in contrast to Guo et al. [44]. The bubbles appear to nucleate out of the bottom of the microchannel but it does not appear to come into much contact with the heated surfaces. Instead, the bubble has the majority of its growth above the fin lands. When the vapor growth is above the channels, the channels walls remain in contact with liquid, which is being displaced by the growing bubble. This is the reason why high heat fluxes are attainable; the liquid is not cut off from the heated surface because of the channels, and with the presence of the liquid, the CHF condition is prevented.

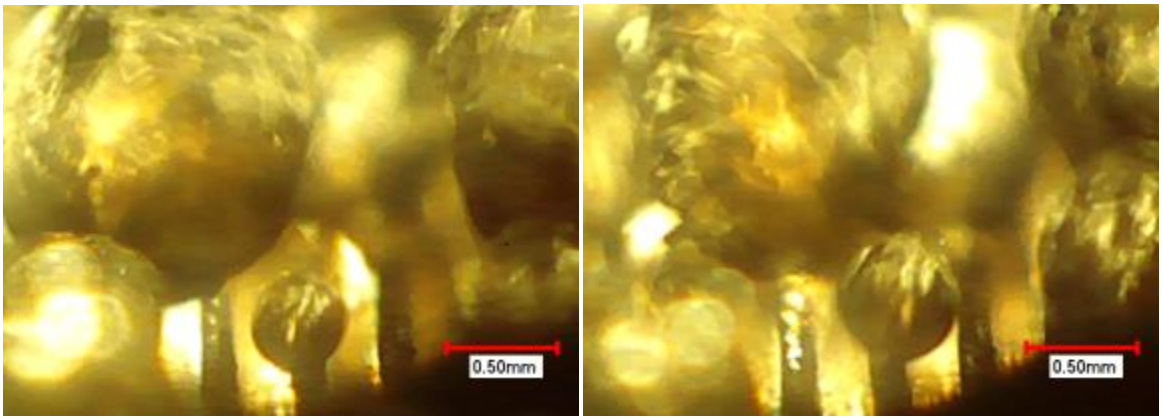

(a) (b)

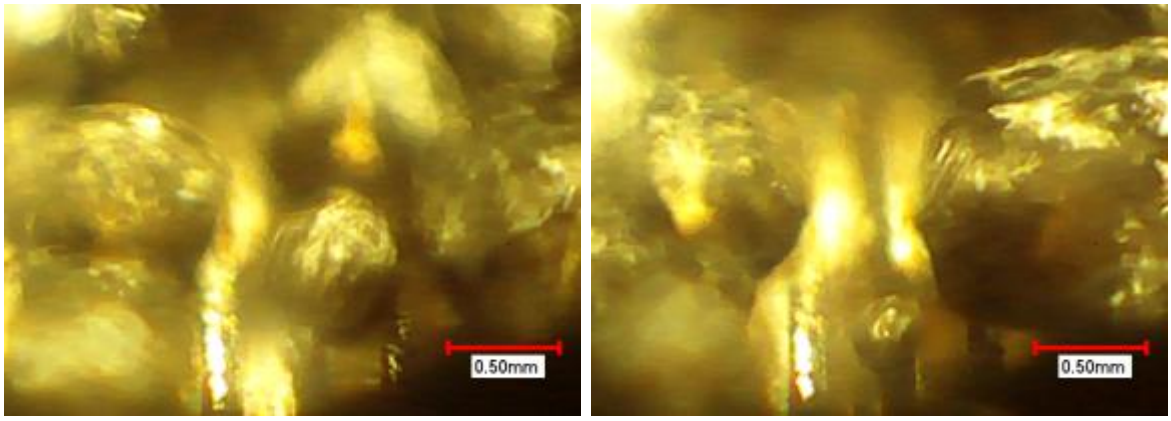

(c) (d)

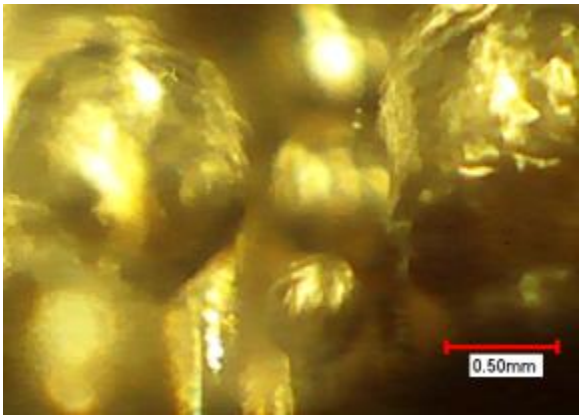

(e)

Figure 6.1. Bubble dynamics on chip 2 at 28 W/cm^2

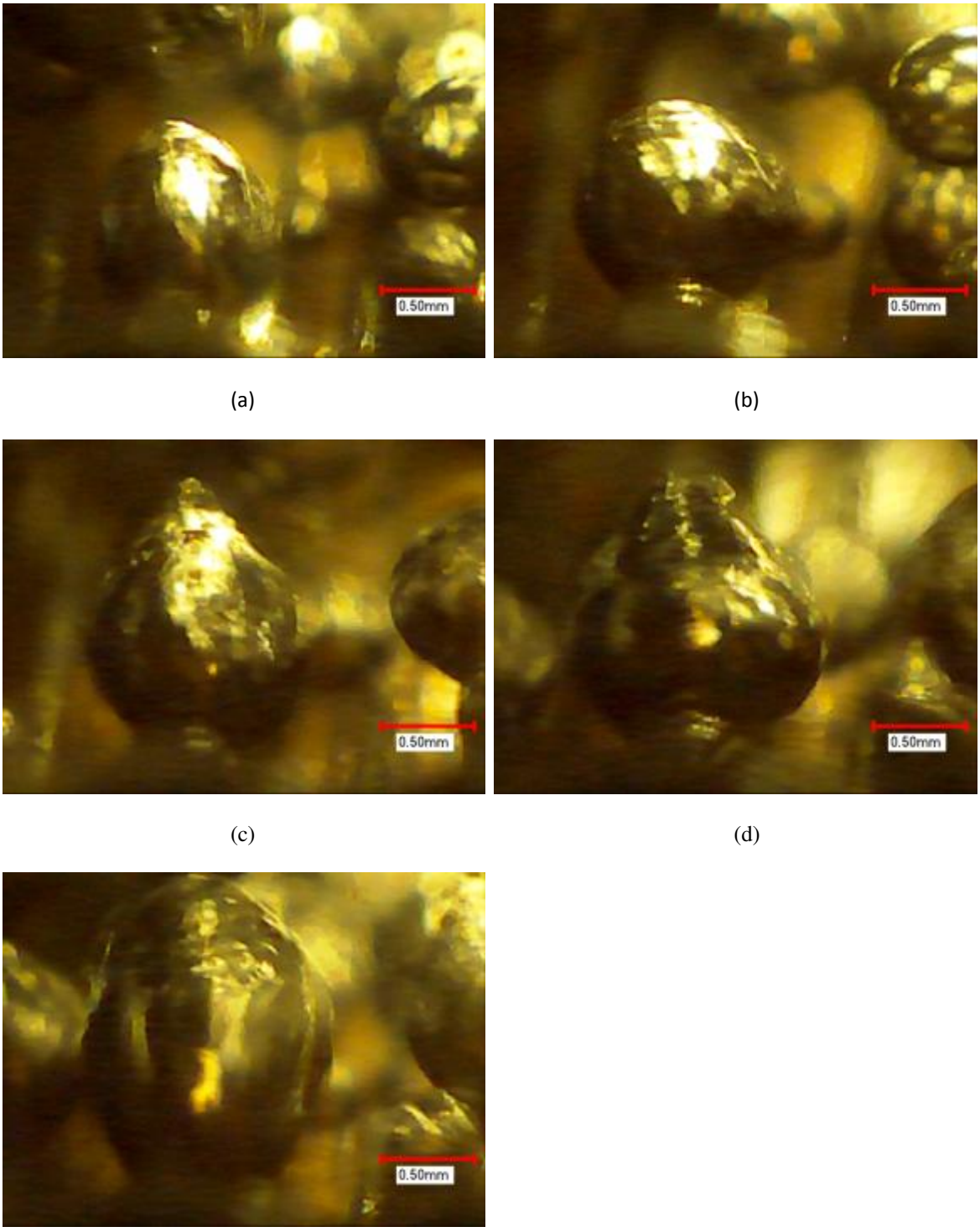

(a) (b)

(c) (d)

(e)

Figure 6.2. High speed video of bubbles nucleating off chip 9 in 2 ms intervals

When the high speed video of chip 9 at 20 W/cm^2 is analyzed, some similarities appear between it and chip 2. Figure 6.2 shows the bubbles nucleating out of the bottom of the channel, most likely out of the corner between the bottom and wall of the channel. That location would act as a crevice that could trap vapor to provide easy bubble growth. The majority of the bubble growth occurs the same way as on chip 2, above the channel. The images also show that the bubble may be tethered to each side of the microchannel wall.

Comparing the high speed videos, the bubbles from chip 2 have been measured to be smaller than the bubbles from chip 9. Although chip 2 has smaller bubbles, nucleation occurs more frequently than chip 9. In order to determine which surface produced more vapor for a given time frame, the bubble departure diameters were measured for the surfaces. The diameter of the bubble as it was departing off the surface was measured by the software from the high speed camera. In the event that a bubble coalesced with vapor from somewhere else in the pool, the diameter of the bubble just before coalescence was used.

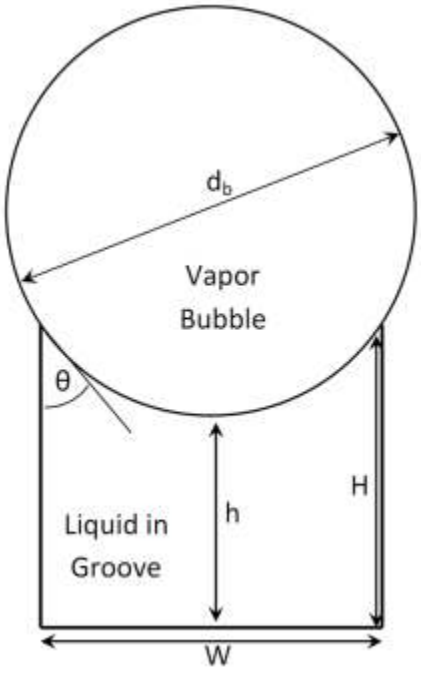

Figure 6.3. Schematic of a bubble above a channel filled with liquid

The bubble departure diameters can be analytically estimated from an analysis of the high speed videos. The videos are able to show the bubbles attached to each side of the channel. An assumption is that the bubble is spherical and there is liquid within the channel. A schematic of this condition is shown in Fig. 6.3. This condition of liquid in a channel is similar to the analysis of Tchikanda et al. [45], which states that the surface between the liquid and vapor will have a constant radius if the channel width is less than the capillary length, defined by $[\gamma/\rho g]^{1/2}$. For water, this length is 2.5 mm. The largest channel is over 5 times smaller than the capillary length, so the assumption can be used. By using the contact angle, θ, the width of the channel W, and the depth of the channel H, the distance from the bottom of the channel to the bubble, h, can be calculated as:

$$h = H + \frac{W}{2}\tan\theta - \sqrt{\frac{W^2}{4\cos^2\theta}} \tag{6.1}$$

After the length to the base of the bubble is calculated, the bubble diameter can be solved for through trigonometric ratios within the bubble. It is simplified down to Eq. 6.2:

$$d_b = \frac{W}{\cos\left(\frac{\pi+\theta}{2}\right)} \tag{6.2}$$

The contact angle of water on a copper chip has been measured in the authors' facility, and resulted in contact angles of 58°, 87°, and 35° for static, advancing and receding conditions, respectively. If the contact angle is taken as 58°, the bubble diameter for chip 2 is calculated as 0.726 mm and for chip 9 the diameter is 1.36 mm. The images in Fig. 6.4 show the contact angle measurement for a water droplet on a copper surface (a), and the measurements for bubble diameter for chips 2 (b) and 9 (c). The images are of isolated bubbles that depart off the surface in the next frame in the video. The diameters of the

bubbles on chips 2 and 9 are larger than the analytical estimate, by about 13%. These numbers should be taken in the context that not all bubbles that depart off the surface are the same size, and are not perfectly spherical for the measurements.

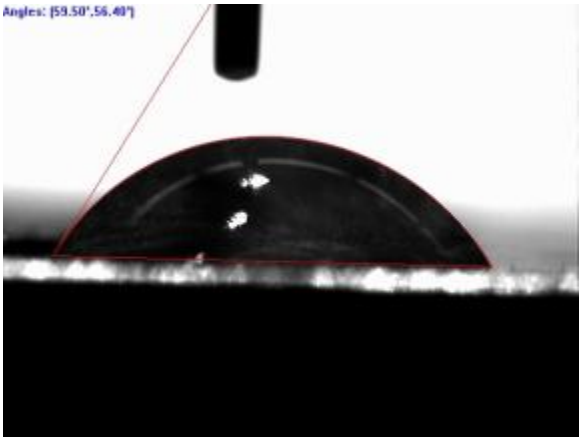

(a)

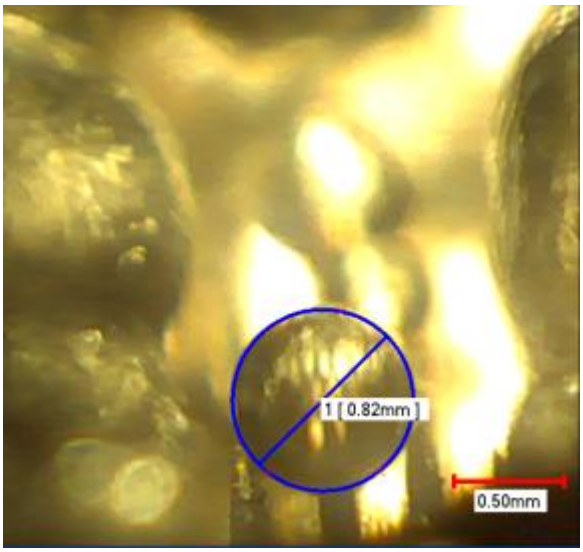

(b)

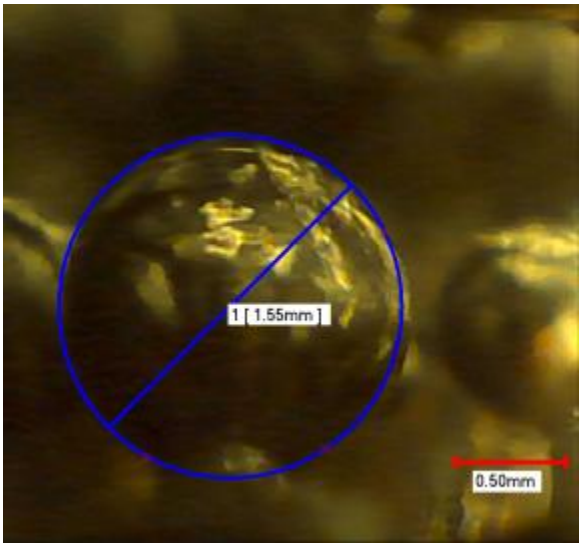

(c)

Figure 6.4. Static contact angle for water on copper (a) bubble departure diameter measurement for chips 2 (b) and 9 (c)

For the segment of video used, chip 2 had a frequency of 143.7 bubbles/second, with a vapor generation rate of 15.6 mm^3/second. For chip 9, which had larger bubble departure diameters, the frequency was 92.0 bubbles/second with a vapor generation rate of 97.2 mm^3/second. This equates to an increase by 6.2 times the vapor generation rate from one nucleation site. For more vapor to be generated, more energy is required so the heat is dissipated without an increase in surface temperature. The actual boiling process is quite a bit more complex with different nucleation site densities and differences in bubble coalescence characteristics, which could not be visualized in the present study.

7. Silicon - Copper Comparison

The boiling curves for the plain silicon and plain copper chips show different heat transfer performance, when looking at the boiling curves in Figs. 4.3 and 5.2. There are several reasons for this difference. Boiling curves are known to shift when using different fluids or surfaces, which is reflected in many correlations, most notably the Rohsenow correlation [4]. The correlation introduces an empirical constant, $C_{s,f}$ which is experimentally determined for various surface-fluid combinations.

Material properties is one factor that contributes to the differences between the silicon and copper surface performance. The thermal conductivity of silicon is approximately 100 W/m°C, while for copper it is four times as much, at 400 W/m°C. This is significant in regards to the heat transfer mechanisms that occur under boiling conditions, in particular, the microlayer evaporation and the transient conduction. During bubble growth, as the vapor interface moves across a heated surface, the temperature of the surface drops due to heat transfer through the microlayer. When the rewetting takes place, the thermal boundary layer is disrupted by cooler liquid from the bulk fluid which contacts the surface. This cooler fluid absorbs heat from the surface, which cools the surface temperature. These two drops in surface temperature have been measured in the study by Moghaddam and Kiger [33].

The heat that is transferred within the surface is greater for the copper surface compared to the silicon surface. The thermal conductivity of copper is 401 W/mK - more than four times that of silicon at 100 W/mK when at a temperature of 100 °C. This means that at the same temperature gradients for the two materials, more heat is transferred in the copper. The same is true for the thermal mass, equivalent to the density multiplied by the

specific heat. Since copper has a larger thermal mass than silicon, for the same temperature difference in the solid, the copper will transfer more heat.

The surface finish on the two materials is different as well. The average roughness values have been measured with a laser confocal microscope. The silicon surface is much smoother, with an average roughness of 0.03 μm while the copper surface has an average roughness value of 0.38 μm. This is important when looking at the requirement for bubble nucleation. Rougher surfaces provide a greater amount of heat transfer because they have more cavities and locations for bubbles to nucleate [4-7, 38, 46]. Since the copper surface used in this study has a higher roughness, the improved performance should be expected.

8. Conclusions

Two different surfaces have been investigated to observe the effect of surface modifications on boiling heat transfer. In the first study, silicon chips were studied to look at the effects of various etched microchannel surfaces. Tested under saturated pool boiling conditions with water as the working fluid at atmospheric pressure, the following heat transfer enhancement patterns emerged.

- All etched surfaces increase the heat transfer compared to a plain chip.
- Microchannel sizes and configurations have an effect. It was found that the offset strip fin geometry had the least amount of enhancement. Also, for surfaces with similar etch depth, the wider channels show better heat transfer. This was shown by comparing the 200 µm wide channels to the 100 µm wide channels.
- Deep channels produce a greater amount of heat transfer at a particular wall superheat. This was demonstrated with 100 µm wide channels, with one chip 275 µm deep outperforming a chip 180 µm deep.
- Normalizing the heat flux by the surface area allows for quantitative analysis by eliminating the effect of increasing the area. The 200 µm wide channeled chips showed that there was still heat transfer enhancement despite the area increase
- High speed video shows that the majority of bubble growth occurs above the microchannels. Although bubbles may nucleate at the bottom of the channel, the majority of the growth occurs when the bubbles are in contact with the fins.

A second study was conducted with copper chips, to further evaluate the heat transfer characteristics of enhanced surfaces with wider and deeper channels. This study evaluated the pool boiling heat transfer performance of microchanneled copper surfaces with 10 different geometries. These surfaces were CNC machined with end mills to create the channels, which were fabricated over a 10 mm x 10 mm area. The heat flux and surface temperature were recorded and used to determine the heat transfer coefficient.

- The chip that had the best performance reached a heat flux of 244 W/cm^2 without reaching CHF and had a heat transfer coefficient of 269 kW/m^2K. This was over 5 times that of the plain chip for the same wall superheat, or 3.7 times that of the maximum heat transfer coefficient of the plain chip.
- This heat transfer coefficient is the largest value seen in the available literature.
- The various geometric parameters that were investigated were the channel width, fin thickness, and depth. It was determined that the best performing chips were those that had wider channels (greater than 350 μm), thinner fins (less than 200 μm), and deep channels (greater than 400 μm).
- The channeled surface acts as a microchannel with three side heating. First, a bubble which nucleates inside a channel grows, pushing liquid away from the nucleation site. This liquid is heated by the surface and channel walls. Next, the vapor grows to the point that it touches both sides of the microchannel to its departure diameter which is dictated by the contact angle and channel width. As a bubble departs out of the channel, cooler liquid at the bulk temperature is pulled into the channel. The volume of the bubble that is evacuated out of the channel must be equal to the volume of fluid which replaces it, so the larger bubbles have a greater effect.

- The data suggests that these factors help in facilitating early bubble nucleation at low wall superheats, larger bubble departure diameters and a higher vapor generation rate in addition to other benefits of a channeled surface for boiling water at atmospheric pressure.
- In this manner of fluid flowing into the channels and towards the nucleation sites, the CHF condition does not readily occur at typical heat fluxes (~100 W/cm^2) reported in literature.

9. Recommendations for Future Work

The heat transfer enhancement developed in this work could be expanded to other operating conditions, while using the same chips. For electronics cooling applications, many researchers have used refrigerants as the working fluid, due to the low boiling point. Electronic devices have a maximum temperature range of 80 - 85 °C, so using a dielectric fluid, or water at reduced pressures with these chips could show enhancement.

Nuclear power generation could also see the benefit from open grooved structures, if new surfaces are developed. Changing from a horizontal heated surface to a circular rod could translate to the nuclear reactor design. These geometries could be refined to dissipate large heat fluxes, without reaching CHF, which would provide massive amounts of power generation without the threat of meltdown. Testing for this application would require the use of water or refrigerants at various pressures, for scaling purposes.

In all of these cases, microstructures, such as nanowires and nanoparticles could be implemented on the surfaces to decrease the contact angle to help keep water in contact with the surface.

10. References

[1] Steinke, M. E., and Kandlikar, S. G., 2006, "Single-Phase Liquid Friction Factors in Microchannels," International Journal of Thermal Sciences, 45(11), pp. 1073-1083.

[2] Incropera, F. P., 2006, Fundamentals of Heat and Mass Transfer, John Wiley \& Sons.

[3] Nukiyama, S., 1934, "Maximum and Minimum Values of Heat Transmitted from Metal to Boiling Water under Atmospheric Pressure," Society of Mechanical Engineers of Japan -- Journal, 37(206), pp. 367-374.

[4] Rohsenow, W. M., 1952, "Method of Correlating Heat-Transfer Data for Surface Boiling of Liquids," American Society of Mechanical Engineers -- Transactions, 74(6), pp. 969-975.

[5] Cooper, M. G., 1984, "Saturation Nucleate Pool Boiling, a Simple Correlation," Proc. First U.K. National Conference on Heat Transfer, 3-5 July 1984, Rugby, UK, pp. 785-93.

[6] Hsu, Y. Y., and Graham, R. W., 1961, "Analytical and Experimental Study of Thermal Boundary Layer and Ebullition Cycle in Nucleate Boiling," National Aeronautics and Space Administration -- Technical Notes, pp. 43.

[7] Hsu, Y. Y., 1961, "On Size Range of Active Nucleation Cavities on Heating Surface," Proc. ASME Meeting WA-177, Nov 26-Dec 1 1961, New York, NY, United States, pp. 7.

[8] Siedel, S., Cioulachtjian, S., and Bonjour, J., 2008, "Experimental Analysis of Bubble Growth, Departure and Interactions During Pool Boiling on Artificial Nucleation Sites," Experimental Thermal and Fluid Science, 32(8), pp. 1504-1511.

[9] Chung, H. J., and No, H. C., 2003, "Simultaneous Visualization of Dry Spots and Bubbles for Pool Boiling of R-113 on a Horizontal Heater," International Journal of Heat and Mass Transfer, 46(12), pp. 2239-2251.

[10] Zhang, L., and Shoji, M., 2003, "Nucleation Site Interaction in Pool Boiling on the Artificial Surface," International Journal of Heat and Mass Transfer, 46(3), pp. 513-522.

[11] Ghiu, C.-D., and Joshi, Y. K., 2005, "Visualization Study of Pool Boiling from Thin Confined Enhanced Structures," International Journal of Heat and Mass Transfer, 48(21-22), pp. 4287-4299.

[12] Mitrovic, J., and Hartmann, F., 2004, "A New Microstructure for Pool Boiling," Superlattices and Microstructures, 35(3-6), pp. 617-628.

[13] Honda, H., and Wei, J. J., 2004, "Enhanced Boiling Heat Transfer from Electronic Components by Use of Surface Microstructures," Experimental Thermal and Fluid Science, 28(2-3), pp. 159-169.

[14] Hübner, P., and Künstler, W., 1997, "Pool Boiling Heat Transfer at Finned Tubes: Influence of Surface Roughness and Shape of the Fins," International Journal of Refrigeration, 20(8), pp. 575-582.

[15] Chang, J. Y., and You, S. M., 1997, "Boiling Heat Transfer Phenomena from Microporous and Porous Surfaces in Saturated Fc-72," International Journal of Heat and Mass Transfer, 40(18), pp. 4437-4447.

[16] Chang, J. Y., and You, S. M., "Enhanced Boiling Heat Transfer from Microporous Surfaces: Effects of a Coating Composition and Method," International Journal of Heat and Mass Transfer, 40(18), pp. 4449-4460.

[17] Hsieh, S.-S., and Weng, C.-J., 1997, "Nucleate Pool Boiling from Coated Surfaces in Saturated R-134a and R-407c," International Journal of Heat and Mass Transfer, 40(3), pp. 519-532.

[18] Rainey, K. N., You, S. M., and Lee, S., 2003, "Effect of Pressure, Subcooling, and Dissolved Gas on Pool Boiling Heat Transfer from Microporous, Square Pin-Finned Surfaces in Fc-72," International Journal of Heat and Mass Transfer, 46(1), pp. 23-35.

[19] Das, A. K., Das, P. K., and Saha, P., 2009, "Performance of Different Structured Surfaces in Nucleate Pool Boiling," Applied Thermal Engineering, 29(17-18), pp. 3643-3653.

[20] Das, A. K., Das, P. K., and Saha, P., 2007, "Nucleate Boiling of Water from Plain and Structured Surfaces," Experimental Thermal and Fluid Science, 31(8), pp. 967-977.

[21] Ramaswamy, C., Joshi, Y., Nakayama, W., and Johnson, W. B., 2003, "Effects of Varying Geometrical Parameters on Boiling from Microfabricated Enhanced Structures," Journal of Heat Transfer, 125(Compendex), pp. 103-109.

[22] Launay, S., Fedorov, A. G., Joshi, Y., Cao, A., and Ajayan, P. M., 2006, "Hybrid Micro-Nano Structured Thermal Interfaces for Pool Boiling Heat Transfer Enhancement," Microelectronics Journal, 37(11), pp. 1158-1164.

[23] Dhir, V. K., and Liaw, S. P., 1989, "Framework for a Unified Model for Nucleate and Transition Pool Boiling," Journal of Heat Transfer, 111(Compendex), pp. 739-746.

[24] Takata, Y., Hidaka, S., Cao, J. M., Nakamura, T., Yamamoto, H., Masuda, M., and Ito, T., 2005, "Effect of Surface Wettability on Boiling and Evaporation," 30, pp. 209-220.

[25] Phan, H. T., Caney, N., Marty, P., Colasson, S., and Gavillet, J., 2009, "Surface Wettability Control by Nanocoating: The Effects on Pool Boiling Heat Transfer and Nucleation Mechanism," International Journal of Heat and Mass Transfer, 52(23-24), pp. 5459-5471.

[26] Chen, R., Lu, M.-C., Srinivasan, V., Wang, Z., Cho, H. H., and Majumdar, A., 2009, "Nanowires for Enhanced Boiling Heat Transfer," Nano Letters, 9(2), pp. 548-553.

[27] Betz, A. R., Xu, J., Qiu, H. H., and Attinger, D., 2010, "Do Surfaces with Mixed Hydrophilic and Hydrophobic Areas Enhance Pool Boiling?," Applied Physics Letters, 97(14).

[28] Chang, J. Y., and You, S. M., 1997, "Boiling Heat Transfer Phenomena from Microporous and Porous Surfaces in Saturated Fc-72," International Journal of Heat and Mass Transfer, 40(18), pp. 4437-4447.

[29] Yang, Y., Ji, X., and Xu, J., 2010, "Pool Boiling Heat Transfer on Copper Foam Covers with Water as Working Fluid," International Journal of Thermal Sciences, 49(7), pp. 1227-1237.

[30] Mori, S., and Okuyama, K., 2009, "Enhancement of the Critical Heat Flux in Saturated Pool Boiling Using Honeycomb Porous Media," International Journal of Multiphase Flow, 35(10), pp. 946-951.

[31] Li, C., and Peterson, G. P., 2007, "Parametric Study of Pool Boiling on Horizontal Highly Conductive Microporous Coated Surfaces," Journal of Heat Transfer, 129(Compendex), pp. 1465-1475.

[32] Judd, R. L., and Hwang, K. S., 1976, "A Comprehensive Model for Nucleate Pool Boiling Heat Transfer Including Microlayer Evaporation," Transactions of the ASME. Series C, Journal of Heat Transfer, 98(Copyright 1977, IEE), pp. 623-9.

[33] Moghaddam, S., and Kiger, K., 2009, "Physical Mechanisms of Heat Transfer During Single Bubble Nucleate Boiling of Fc-72 under Saturation Conditions-I. Experimental Investigation," International Journal of Heat and Mass Transfer, 52(Copyright 2009, The Institution of Engineering and Technology), pp. 1284-94.

[34] Zuber, N., 1959, "Hydrodynamic Aspects of Boiling Heat Transfer," University of California at Los Angeles.

[35] Haramura, Y., and Katto, Y., 1983, "A New Hydrodynamic Model of Critical Heat Flux, Applicable Widely to Both Pool and Forced Convection Boiling on Submerged Bodies in Saturated Liquids," International Journal of Heat and Mass Transfer, 26(Copyright 1983, IEE), pp. 389-99.

[36] Moissis, R., and Berenson, P. J., 1963, "On Hydrodynamic Transitions in Nucleate Boiling," American Society of Mechanical Engineers -- Transactions -- Journal of Heat Transfer, 85(3), pp. 221-229.

[37] Kandlikar, S. G., 2010, "A Scale Analysis Based Theoretical Force Balance Model for Critical Heat Flux (Chf) During Saturated Flow Boiling in Microchannels and Minichannels," Journal of Heat Transfer, 132(8), pp. 081501-13.

[38] Kandlikar, S., G., and Spiesman, P., H., 1997, "Effect of Surface Characteristics on Flow Boiling Heat Transfer," Proc. Engineering Foundation Conference on Convective Flow and Pool Boiling, Irsee, Germant.

[39] Mchale, J. P., and Garimella, S. V., 2010, "Bubble Nucleation Characteristics in Pool Boiling of a Wetting Liquid on Smooth and Rough Surfaces," International Journal of Multiphase Flow, 36(4), pp. 249-260.

[40] Cooke, D., and Kandlikar, S. G., 2011, "Pool Boiling Heat Transfer and Bubble Dynamics over Plain and Enhanced Microchannels," Journal of Heat Transfer, 133(5), pp. 052902-9.

[41] Rohsenow, W. M., and Griffith, P., 1956, "Correlation of Maximum Heat Transfer Data for Boiling of Saturated Liquids," Chem. Eng. Prog., 52(

[42] Kandlikar, S. G., 2001, "A Theoretical Model to Predict Pool Boiling Chf Incorporating Effects of Contact Angle and Orientation," Transactions of the ASME. Journal of Heat Transfer, 123(Copyright 2002, IEE), pp. 1071-9.

[43] Kandlikar, S. G., 2006, Heat Transfer and Fluid Flow in Minichannels and Microchannels, Elsevier Science Ltd, Oxford.

[44] Guo, C., Hu, X., Wu, L., Tang, D., and Wang, T., 2009, "Analysis of Micro Vapor Bubble Growing Process in Open Capillary Microgrooves," Proc. 7th International Conference on Nanochannels, Microchannels, and Minichannels, ICNMM2009, June 22, 2009 - June 24, 2009, Pohang, Korea, Republic of, pp. 595-601.

[45] Tchikanda, S. W., Nilson, R. H., and Griffiths, S. K., 2004, "Modeling of Pressure and Shear-Driven Flows in Open Rectangular Microchannels," International Journal of Heat and Mass Transfer, 47(3), pp. 527-538.

[46] Kandlikar, S. G., 1999, Handbook of Phase Change: Boiling and Condensation, Taylor & Francis, Philadelphia, Chap. 15.